A scalable, all-optical method for mapping synaptic connectivity with cell-type specificity

Maria V. Moya[1,2], William J. Cunningham[3,4], Jack P. Vincent[1,4], Tim Wang[5], Michael N. Economo[1,2,4]

[1]*Department of Biomedical Engineering, Boston University, Boston, MA.*
[2]*Center for Systems Neuroscience, Boston University, Boston, MA.*
[3]*Graduate Program for Neuroscience, Boston University, Boston, MA.*
[4]*Center for Neurophotonics, Boston University, Boston, MA.*
[5]*Allen Institute for Neural Dynamics, Seattle, WA.*

Correspondence: mne@bu.edu

ABSTRACT

Single-cell transcriptomics has uncovered the enormous heterogeneity of cell types that compose each region of the mammalian brain, but describing how such diverse types connect to form functional circuits has remained challenging. Current methods for measuring the probability and strength of cell-type specific connectivity motifs principally rely on low-throughput whole-cell recording approaches. The recent development of optical tools for perturbing and observing neural circuit activity, now notably including genetically encoded voltage indicators, presents an exciting opportunity to employ optical methods to greatly increase the throughput with which circuit connectivity can be mapped physiologically. At the same time, advances in spatial transcriptomics now enable the identification of cell types *in situ* based on their unique gene expression signatures. Here, we demonstrate how long-range synaptic connectivity can be assayed optically with high sensitivity, high throughput, and cell-type specificity. We apply this approach in the motor cortex to examine cell-type-specific synaptic innervation patterns of long-range thalamic and contralateral input onto more than 1000 motor cortical neurons. We find that even cell types occupying the same cortical lamina receive vastly different levels of synaptic input, a finding which was previously not possible to uncover using lower-throughput approaches that can only describe the connectivity of broad cell types.

INTRODUCTION

The function of a neural circuit is intimately related to its structure. Neuroanatomy has been instrumental for inspiring conceptual ideas and constraining computational models of circuit function in the mammalian cerebellum, hippocampus, basal ganglia, neocortex, and retina, among other areas[1–9].

Classically, the cellular building blocks of neural circuits have been identified and described in a painstaking fashion through a synthesis of information about their location, morphology, gene expression, electrophysiological characteristics, and patterns of activation during behavior. Identifying the connectivity motifs that govern how different types of cells integrate into larger circuits and connect distant regions has been an equally challenging endeavor. The proliferation of large-scale, single-cell transcriptomic data has been transformative for efforts to catalogue cell types across brain areas. Importantly, these data now suggest a much higher degree of cell type diversity than previously appreciated in most brain regions[10,11]. The rapid pace of progress in our understanding of the diversity of neuronal cell types has also now surpassed our ability to determine their local and long-range connectivity at a commensurate level of detail. Thus, our ability to effectively leverage these advances into new insights about neural computation is limited.

This disconnect is due to a lack of scalable methods for determining the probability and strength of connections between the large numbers of transcriptomically defined cell types comprising neural circuits. Electron microscopy (EM) and transsynaptic tracers are commonly used to identify synaptic connections and are potentially scalable[12–18]. However, long-range connections into and out of EM tissue volumes are severed, cell types are difficult to identify, and it is challenging to estimate connection strengths from

ultrastructure alone. Similarly, transsynaptic tracing cannot report connection strengths and typically have high and/or cell-type specific false negative rates that are difficult to characterize. Alternatively, synaptic connectivity can be identified functionally using patch-clamp electrophysiology. For instance, 'paired-patch' electrophysiology has been used extensively for measuring local connectivity between pairs of neurons[19–21]. Similarly, to identify long-range inputs, Channelrhodopsin-assisted circuit mapping (CRACM) integrates optogenetic activation of axonal fibers and patch-clamp electrophysiology[22,23]. However, paradigms involving patch-clamp electrophysiology are labor intensive and difficult to scale for assaying all cell types.

Thus, we sought to develop a method for assaying synaptic connectivity that is (1) highly scalable and (2) compatible with measurements of gene expression for cell type identification. We demonstrate that synaptic potentials can be detected in a sensitive and highly parallel manner across populations of neurons using genetically encoded voltage indicators (GEVIs), presenting a high-throughput alternative to patch-clamp electrophysiology for connectivity measurements. Integrating optogenetic control of presynaptic release with population GEVI imaging of synaptic potentials yields Optical Circuit Mapping (OCM), a scalable method for assessing connectivity. OCM can be readily combined with multiplexed fluorescence in situ hybridization (mFISH) for scalable cell type identification to provide a high-throughput method for mapping connectivity between transcriptomically defined cell types (OCM-FISH). We apply OCM-FISH to map long-range thalamic and homotypic callosal inputs onto over 1000 transcriptomically identified cells in the motor cortex. Surprisingly, we find that long-range inputs are integrated with a high degree of cell-type specificity such that cell types occupying the same cortical lamina are often selectively targeted in a pathway-specific manner.

RESULTS

Sensitive and scalable optical detection of synaptic potentials with OCM

In OCM, optically evoked postsynaptic potentials (PSPs) are detected across populations of neurons in a parallel fashion using fluorescence imaging of genetically encoded voltage indicators (GEVIs). To determine whether PSPs could be detected with simple widefield GEVI imaging, we expressed the blue-shifted opsin, CheRiff[24], in cells in ventromedial and ventroanterolateral nuclei (VM and VAL) of the motor thalamus (MThal) and the chemigenetic GEVI, Voltron2[25], sparsely (2-5% of neurons) across the anterior-to-posterior extent of the primary motor cortex (**Fig. 1a,b**). We performed simultaneous whole-cell electrophysiology and voltage imaging in Voltron2-expressing neurons while optically activating CheRiff-expressing MThal axons to elicit subthreshold responses in the motor cortex *in vitro* (**Fig. 1c,d**). Labeling Voltron2 with the dye JaneliaFluor 585[26] ($Voltron2_{JF585}$) allowed spectrally separable voltage imaging and optogenetic activation.

Simultaneous GEVI measurements of optically evoked PSPs were noisy, such that millivolt-scale PSPs could not be reliably detected on single trials (**Fig. 1e**). However, averaging optical measurements across repeated photostimuli reduced noise, revealing PSPs (**Fig. 1e**). To calibrate optical voltage measurements across cells of varying Voltron2 expression levels, we characterized the fluorescence-voltage (F-V) relationship while measuring voltage simultaneously with GEVI imaging and patch clamp electrophysiology. For all cells, this relationship was linear with a median slope of -0.27%/mV (**Fig. 1f**; IQR -0.38 to -0.20%; n = 11), as expected for the negative-going Voltron2 GEVI[25]. Based on the F-V relationship and noise level measured in each cell, we calculated the minimum PSP amplitude detectable after averaging across photostimuli. The median threshold for PSP detection (PSP amplitude z-score ≤ -2.576) was 0.35 mV (IQR 0.23 to 0.53 mV; n = 11) and was less than 1 mV in all cells assayed (**Fig. 1g**). In some cells, trial-averaging produced high enough SNR to readily detect a range of response amplitudes, even those nearing 0.25 mV in amplitude (**Fig. 1h**). Optically measured PSPs were abolished in all cells upon pharmacological block of glutamatergic synaptic transmission with NBQX and AP-5 (10 μM each; **Fig. 1i**), as expected. These results indicate that PSPs can be both optically elicited from presynaptic

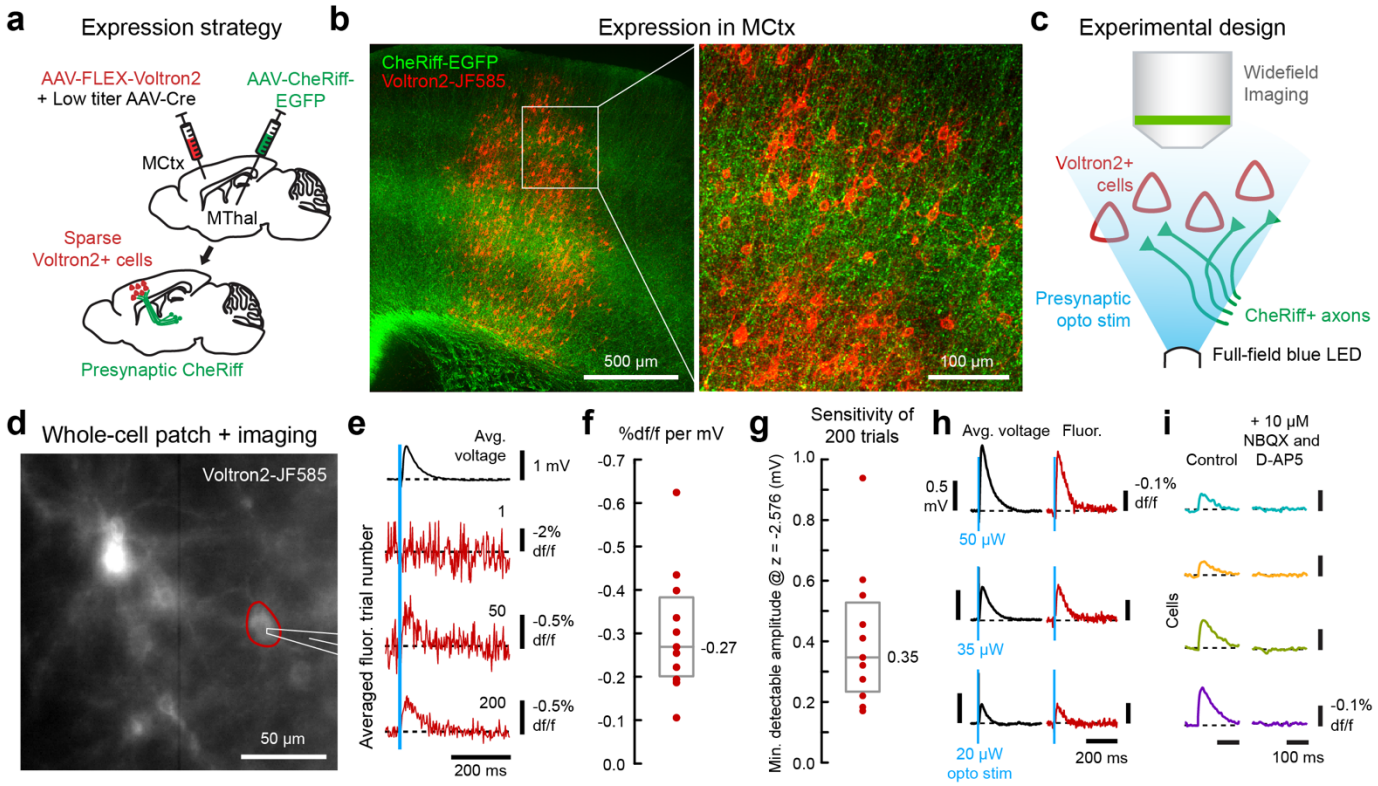

Figure 1 – Sensitivity of optical circuit mapping for detection of postsynaptic potentials. (***a***) Schematic showing viral delivery and expression strategy for targeting CheRiff-EGFP to presynaptic neurons in the motor thalamus (MThal) and for sparsely expressing Voltron2 in postsynaptic neurons in the primary motor cortex. (***b***) Z-projected confocal image and inset of CheRiff-EGFP-positive MThal axons (green) and Voltron2-JF585-positive neurons (red) across 10 µm of motor cortex. (***c***) Schematic showing the experimental design for optical circuit mapping (OCM). Acute slices containing CheRiff-positive MThal axons and Voltron2-expressing neurons are imaged on a widefield microscope. Presynaptic MThal axons are activated using a full-field blue LED. (***d***) Widefield image of Voltron2-JF585 signal in an acute slice, with a Voltron2-positive neuron (red) patched for simultaneous whole-cell recording. White lines highlight location of patch pipette. (***e***) Postsynaptic potentials (PSPs) measured using whole-cell voltage recording (top, black) and fluorescent timeseries extracted from cell in ***d*** (red outline and traces). Averaging PSP profiles across repetitive photoactivation trials (1, 50, and 200 trial-averages are shown) increases the response signal-to-noise. (***f***) Box and whisker plot showing the percent change in fluorescence observed for Voltron2-JF585 for a 1 mV change in membrane voltage across all cells patched (red dots; n = 11; median = -0.27%, IQR -0.38 to -0.20%). (***g***) Box and whisker plot showing the minimum PSP amplitude detectable (with statistical confidence, $z \leq -2.576$) over noise when averaging 200 photoactivation trials across all cells patched (red dots; n = 11; median = 0.35 mV, IQR 0.23 to 0.53 mV). (***h***) Whole-cell (black) and fluorescent (red) traces from one patched neuron showing that PSP amplitude can be modulated by employing differing stim LED intensities during OCM. (***i***) Trial-averaged traces from 4 neurons in the same field-of-view of an OCM experiment, showing that responses are abolished in the presence of glutamatergic blockers (10 µM NBQX and D-AP5), confirming their synaptic origin.

terminals and optically detected in postsynaptic neurons with sufficient sensitivity to effectively measure synaptic connectivity. To map presynaptic inputs to a population of motor cortical cells, we applied OCM across multiple fields-of-view (**Fig. 2a**) in the presence of tetrodotoxin (TTX) to prevent multisynaptic activation and 4-Aminopyridine (4-AP) to enhance pre-synaptic excitability[27], as in CRACM[23]. PSPs resulting from photoactivation of CheRiff-expressing axons from the contralateral motor cortex (Contra) could be assayed across hundreds of cells in single experiments (**Fig. 2b**). Intermingled cells exhibited heterogeneous responses to presynaptic axon photoactivation (**Fig. 2a,b**), with some exhibiting large-amplitude PSPs and others responding minimally, or not at all (**Fig. 2b,c**). Cells with PSP amplitudes significantly greater than their baseline noise were classified as 'responding' cells (see **Supplementary Note 1**). Across these cells, we observed a mean response amplitude of -0.93 ± 0.23% df/f (SEM; estimated 3.44 mV ± 0.85 mV), with a maximum PSP size of -6.72% df/f (estimated 25.89 mV). This is consistent with previously reported response sizes in the cortex following optogenetic photoactivation of an entire input pathway, which are typically 2-10 mV but can be up to 25 mV depending on the laminar position of the sampled neuron, the photoactivation strength used, and opsin expression and targeting[28–30].

These findings confirm that the presence and strength of long-range synaptic connections can be identified with high sensitivity using OCM, much like in CRACM. Parallelizing detection with GEVI imaging dramatically increases the scalability of PSP detection.

Transcriptomic cell type identification in thick tissue sections

We next developed an approach for determining the transcriptomic type of neurons interrogated with OCM based on their pattern of gene expression. We optimized a multi-round protocol for multiplexed fluorescence in situ hybridization (mFISH) using hybridization chain reaction version three (HCRv3; **EDFig. 2a**)[31] that could be used to detect transcripts associated with cortical cell type marker genes. In this protocol, endogenous CheRiff-EGFP fluorescence (**EDFig. 2b**) could be quenched chemically, and high signal-to-background could be maintained throughout the thickness of 300-µm, paraformaldehyde-fixed tissue sections (**EDFig. 2c,d**), as well as across multiple rounds of staining (**EDFig. 3**). Using the Allen Institute ABC atlas single-cell RNA sequencing (scRNA-Seq) data[11], we selected a set of 17 genes whose expression differentiates motor cortical cell types (**EDFig. 4a**). This set incorporated marker genes commonly associated with both broad excitatory (*Rorb, Lratd2, Npnt, Slco2a1, Syt6*) and inhibitory (*Slc32a1, Pvalb, Sst, Vip, Lamp5*) cortical cell types, as well as additional differentially expressed genes that further distinguish excitatory types at a finer resolution (*Penk, Calb1, Pamr1, Dkkl1, Ccdc80, Myl4*; **EDFig. 4c**). In each of 4 rounds of staining, transcripts associated with 4 marker genes were visualized (**Fig. 3a**). A fifth gene, the pan-neuronal marker gene *Snap25,* was also included in all rounds of staining to ensure that RNA integrity was maintained across rounds and to facilitate computational analyses.

We next developed a computational pipeline for classifying cell types using multi-round mFISH image data. First, *Snap25* signal was used for across-round image registration (**EDFig. 3**) and for cell segmentation (**EDFig. 5a**). Second, expression of each gene in mFISH data was evaluated in a binary fashion (i.e., expressed/not expressed) across cells to produce a 17-digit binary expression code for each cell that could be related to known type-specific expression patterns in the ABC atlas cell type ontology. Notably, low-depth scRNA-Seq data yield noisy estimates of the expression of individual genes at the single-cell level. For this reason, marker genes often did not display expected bimodal expression patterns at the level of single neurons in scRNA-Seq data (**EDFig. 4b**). For example, the expression of *Slc32a1*, encoding the GABA transporter did not follow the expected bimodal distribution of expression across neurons that follows from its specific expression in inhibitory, but not excitatory, neurons. To mitigate this problem, and motivated by an expected ~10% RNA capture rate in scRNA-Seq data, we replaced each scRNA-Seq cell with a "meta cell" representing its expression counts summed with the expression counts of its 9 nearest-neighbor cells of the same transcriptomic "supertype" in PCA space. A bimodality (or trimodality) in

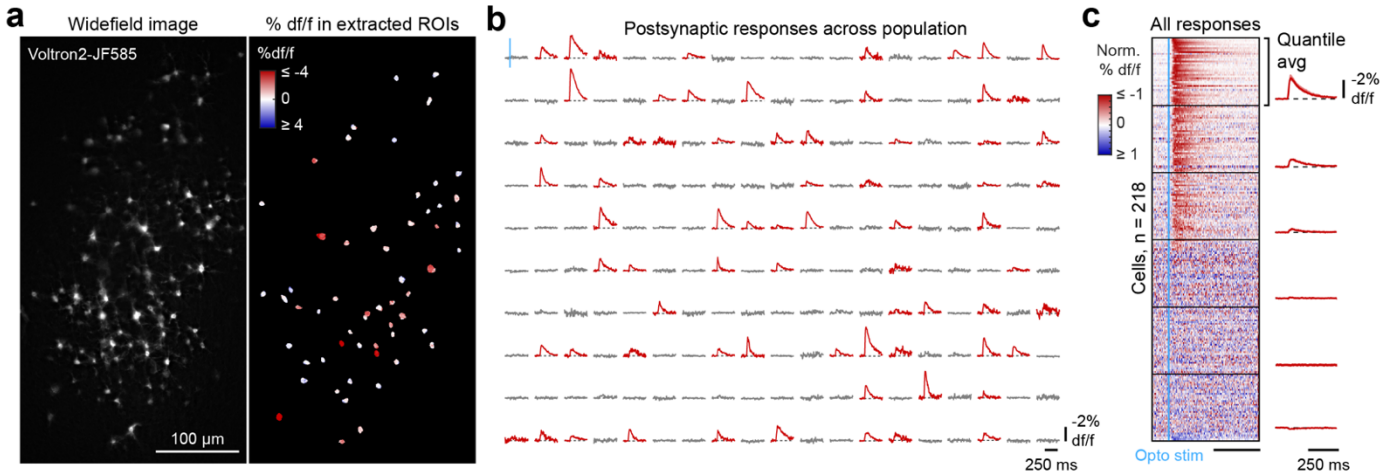

Figure 2 – OCM provides large-scale connectivity data across a whole population of neurons. (***a***) Representative widefield image of an OCM field-of-view spanning multiple cortical layers (left), with spatial heatmap of PSP amplitude (% df/f) measured for individual cell ROIs (right) in response to contralateral motor cortex (Contra) axon activation. (***b***) PSP timeseries measured across 190 neurons in one experiment, showing responding (red) and non-responding (grey) cells. (***c***) Heatmap showing PSP timeseries normalized to the maximum value in the response window across individual cells (rows) imaged in same experiment as ***b*** (left), ordered by response amplitude, with average PSP traces for each quantile of the population (right; shaded region shows 95% CI).

147

marker gene expression was revealed in meta cell data (**EDFig. 4b**). Marker gene expression across meta cells was then binarized (**EDFig. 4b**) to facilitate comparison with binarized mFISH expression patterns.

We used these data to calculate the proportion of each cell type expressing each gene, and determined the proportion of each cell type at each cortical depth in Allen Institute ABC atlas MERFISH dataset[11] (**EDFig. 6a-c**) to construct a naïve Bayes classifier for identifying mFISH cells based on gene expression and a depth-dependent cell type prior. To determine whether gene expression patterns alone were sufficient for appropriately classifying cells to the ABC "supertype" level for excitatory cells and "subclass" level for inhibitory cells, we compared cell types identified by the classifier in a representative tissue section when depth-dependent prior probabilities were either excluded or included (**Fig. 3b-d, EDFig. 6e**; n = 14,483 cells). We found that each identified cell type largely followed expected laminar distributions in both cases, with the exception of L6 intratelencephalic (IT) neurons whose classification further benefitted from including depth-dependent priors (**Fig. 3d, EDFig. 6a,b**). Including depth-dependent priors additionally resulted in a classified population that matched reference ABC atlas types in terms of their overall prevalence as well as expression patterns (**Fig. 3c,d, EDFig. 7**). These results indicate that the expression patterns of our 17 selected marker genes along with laminar depth can successfully differentiate taxonomic excitatory supertypes and inhibitory subclasses in mFISH data.

OCM-FISH: Integrating optical circuit mapping with transcriptomic cell type identification

We next integrated OCM with mFISH-based transcriptomic cell type identification (**Fig. 4a**) to determine if and how long-range inputs are integrated in the motor cortex in a cell-type specific manner. We first determined whether Voltron2 could be effectively expressed broadly across cell types via AAV injection. As expected, the tropism across cell types of AAV infection was serotype dependent (**Fig. 4b-d**). We found that Voltron2 expression via AAV5 yielded good coverage across cell types (**Fig. 4d**) and selected this serotype for subsequent experiments. We then expressed Voltron2 in motor cortex cells and CheRiff in either MThal (**EDFig. 8a**) or Contra (**EDFig. 8b**) – two of the most prominent sources of afferent input to motor cortical neurons – and used OCM to identify neurons receiving synaptic connections from these sources. The distribution of axonal CheRiff across cortical lamina was similar when CheRiff was expressed in MThal or Contra (**EDFig. 8c,d**), with the notable exception of layer 1, which contained a high density of MThal, but not Contra, axonal labeling. Using widefield OCM, we mapped MThal input (n = 2 animals; **Fig. 4e**) and Contra input (n = 2 animals; **Fig. 4f**) onto a large population of motor cortex cells across approximately 50 µm from the slice face.

Following OCM, brain slices were fixed and high-resolution confocal images were acquired to verify that Voltron2-expressing neurons were located within the terminal zone of CheRiff-expressing axons and to facilitate registration of widefield GEVI imaging with post-hoc mFISH confocal imaging data (**EDFig. 9a**). Gene expression was then evaluated using our multi-round mFISH protocol. Cells were segmented using an image containing *Snap25* signal, as before (**ED Fig. 5**), but only Voltron2-positive cell masks were included for further characterization (**EDFig. 9b**). A subset of Voltron2-expressing cells (18%) lacked detectable mRNA (likely due to cellular stress caused by overexpression of Voltron2 and/or mechanical damage) and were therefore excluded from subsequent analyses. Following OCM and 17-plex mFISH, the connectivity and cell type of 794 (MThal) and 344 (Contra) neurons was identified using our classifier (**Fig. 4e,f**). Importantly, the sampled populations showed similar cell type composition across both circuits, with all excitatory supertypes and inhibitory subclasses represented in both datasets.

Postsynaptic potentials were detected in 251/794 cortical cells (31.5%) upon MThal axon photoactivation and 196/344 cortical cells (57.0%) upon Contra axon photoactivation. PSPs detected in response to photoactivation of Contra axons were additionally larger in amplitude (MThal: -0.28 ± 0.04%, estimated 1.04 ± 0.15 mV; Contra: -0.80 ± 0.17%, estimated 2.96 ± 0.63 mV) although the response probability and absolute amplitude of PSPs in this paradigm depends on the proportion of presynaptic terminals that are

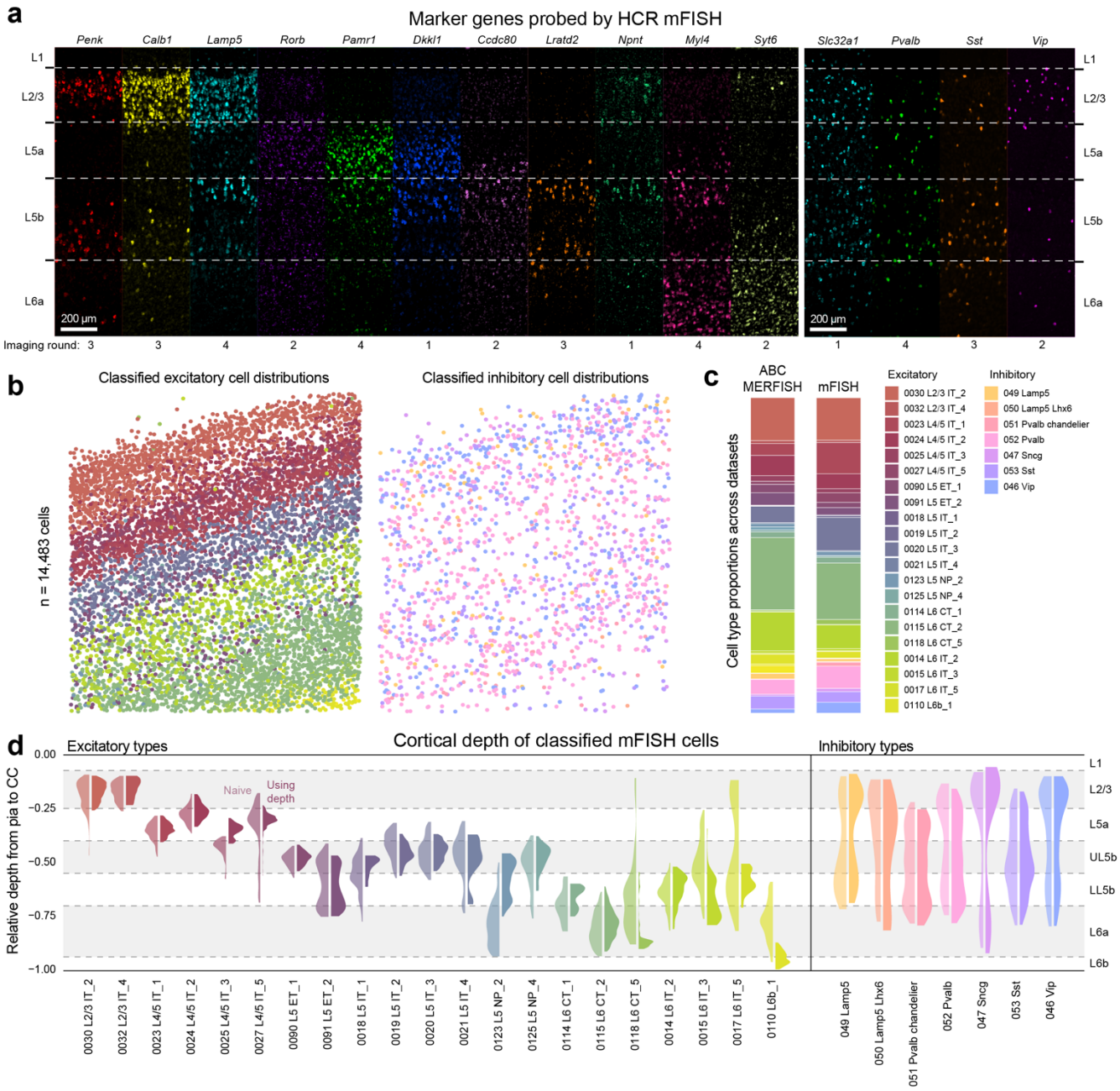

Figure 3 – Cell type classification using thick-tissue mFISH data. (***a***) Confocal images of a subset of excitatory and inhibitory marker genes probed by HCR mFISH in one tissue section across 4 rounds of staining. (***b***) Scatterplots showing motor cortex cells (dots) imaged across 50 µm of z-depth in multi-round mFISH and classified into excitatory (left) or inhibitory (right) cell types based on gene expression patterns (n = 14,483 cells). Cell types were determined using a classifier that included depth-dependent cell type priors and ABC scRNA-Seq "meta cell" gene expression probabilities. (***c***) Stacked bar plots showing the cell-type composition of ABC MERFISH motor cortex data (left) and the mFISH-based classification (right) for data shown in ***b***. (***d***) Violin plots of the laminar distribution of excitatory and inhibitory cell types classified from mFISH data shown in ***b*** and ***c***– without using ("naïve"; left half of violin) or using (right half of violin) depth-dependent cell type priors. Distributions show cells between the 5th and 95th percentiles of depth.

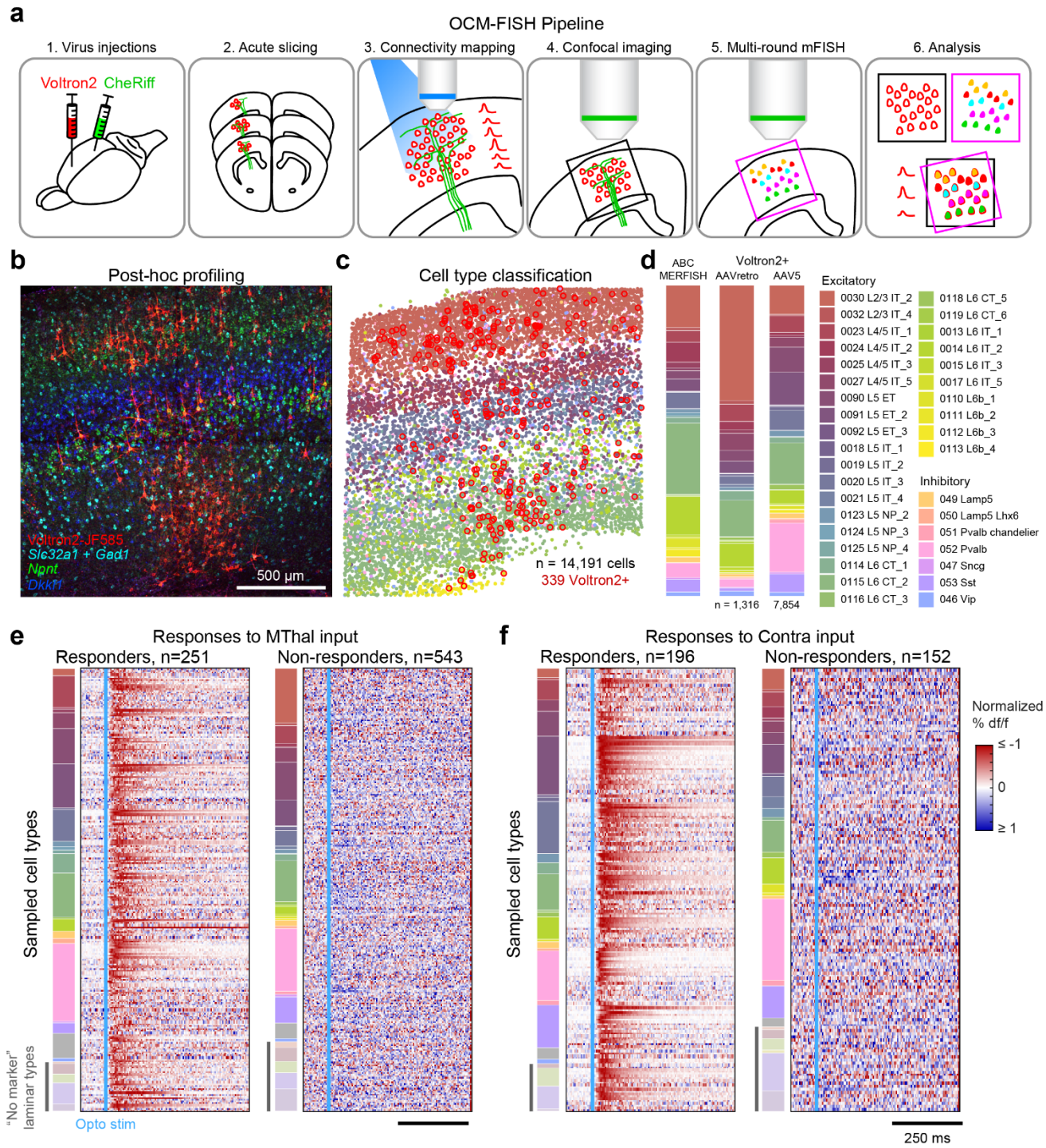

Figure 4 – Combined OCM-FISH pipeline provides cell type-specific connectivity data. (***a***) Schematic outline of complete OCM-FISH pipeline. (***b***) Confocal image of HCR mFISH performed in Voltron2-expressing motor cortex. (***c***) Scatterplot showing motor cortex cells (dots) imaged across 50 µm of z-depth in multi-round mFISH and classified into excitatory or inhibitory cell types (n = 14,191 cells). Voltron2-expressing cells (n = 339 cells) are highlighted with red circles. (***d***) Stacked bar plots showing the cell-type composition of ABC MERFISH data (left), and the Voltron2-expressing population when the Cre transgene is delivered using either the AAVretro (center, n = 2 animals) or AAV5 (right, n = 4 animals) serotype. (***e, f***) Heatmaps showing PSP timeseries normalized to the maximum value in the response window across individual responding (left) and non-responding (right) cells (rows) imaged in OCM-FISH experiments mapping MThal input (***e***; n = 2 animals, 794 cells) or contra motor cortex input (***f***; n = 2 animals, 348 cells) onto motor cortex. Rows ordered first by cell type (highlighted in stacked bar to the left) and then by PSP amplitude. Cells with no detectable mFISH markers (i.e., "No marker" laminar types) highlighted with grey bar.

labeled with CheRiff in each pathway as well as the expression level of the opsin in each group of axons. MThal and Contra inputs both targeted cells in all motor cortical laminae, although the laminar specificity of each pathway differed markedly, with MThal axons targeting cells in middle laminae, particularly L5b, and Contra axons most strongly targeting cells in L6 (**Fig. 5a,c**). We next examined whether MThal and Contra axons innervated cells indiscriminately based on their laminar position, or whether they targeted particular cell types specifically. Cell types defined at the relatively broad ABC "subclass" level in laminae 5 and 6, which MThal axons targeted most strongly, did not display a high degree of heterogeneity in the degree to which they received MThal input (**Fig. 5a**). However, when broad classes were subdivided further into ABC "supertypes", substantial cell-type specificity was revealed (**Fig. 5b**). For example, MThal input to the dominant cell types in upper layer 5b was highly specific. Input to the "0020 L5 IT_3" supertype– a *Dkkl1*- and *Ccdc80*-positive L5 IT cell type– was 4.5x stronger than to the "0090 L5 ET_1" supertype– representing the thalamic-projecting ET type– (0020: -0.77% ± 0.31%, n = 37; 0090: -0.19% ± 0.08%, n = 66; p = p < 0.0001, two-tailed t-test), despite both types having indistinguishable laminar distributions. The two dominant excitatory supertypes in L5a – the *Pamr1*- and *Dkkl1*-positive "0023 L4/5 IT_1" and the *Pamr1*- and *Dkkl1*-negative "0027 L4/5 IT_5" intratelencephalic types– also received MThal input that was different in strength (0023: -0.44% ± 0.15%, n = 40; 0027: -0.28% ± 0.15%, n = 27; p < 0.0001). Importantly, normalizing each cell's PSP amplitude to CheRiff intensity in its cortical column maintained relative differences in response strength across cell types (**ED Fig. 10**), ruling out the possibility that variable innervation density across columns drove the differences in response strength.

Synaptic potentials resulting from Contra axon photoactivation were larger in deeper cortical lamina (**Fig. 5c**). For example, Pvalb- and Sst-positive interneurons in L6a showed greater response amplitudes to Contra input (-2.00 ± 0.86%, n = 13; -2.00 ± 0.95%, n = 7) compared to Pvalb- and Sst- cells in L5a (-0.37 ± 0.31%, n = 10; -0.58 ± 0.46%, n = 7; **EDFig. 11b**). At the relatively broad "subclass" level, L5 and 6 cell types showed heterogenous responses to Contra input (**Fig. 5c**). Further breaking down these broad classes into more finely delineated "supertypes" again revealed substantial specificity (**Fig. 5d**). For example, the "0020 L5 IT_3" supertype received 1.8x stronger input (-0.85 ± 0.31%, n = 30) than the "0090 L5 ET_1" supertype (-0.47 ± 0.21%, n = 15; p < 0.0001) which occupies the same upper L5b (UL5b) sublamina. In the deeper lower L5b (LL5b) sublamina, the "0091 L5 ET_2" supertype – representing the medulla- and spinal-projecting ET cells– similarly received 1.7x stronger input than the *Lamp5*- and *Myl4*-positive "0114 L6 CT_1" supertype (0091: -1.93 ± 0.53%, n = 36; 0114: -1.12 ± 0.45%, n = 6; p = 0.001).

The absolute magnitude of PSPs resulting from MThal and Contra axon photoactivation were indistinguishable in IT cells in lamina 2/3 and 5a, but clearly diverged in all ET and CT types (**Fig. 5e**). These latter types received much stronger input from Contra axons than MThal axons, despite the overall similarity in the laminar profile of axonal labeling across these pathways, suggesting that targeting of postsynaptic cell types was highly pathway-specific. Interestingly, both MThal and Contra input targeted L5b ET_2 neurons much more strongly than ET_1 neurons (MThal – ET_1: -0.19 ± 0.08%, n = 66; ET_2: -0.36 ± 0.14%, n = 57; p < 0.0001; Contra – ET_1: -0.47 ± 0.21%, n = 15; ET_2: -1.93 ± 0.53%, n = 36; p < 0.0001), potentially accounting for the stronger modulation of medulla- and spinal-projecting ET_2 neuron activity compared to thalamic-projecting ET_1 neurons in the motor cortex when animals initiate movement[32]. Together, these data suggest a high degree of specificity in afferent connectivity across pathways and cell types, which would have been difficult to observe without the high throughput and cell-type specificity provided by OCM-FISH.

DISCUSSION

Many regions of the mammalian brain contain a high diversity of cell types, and in most regions, the wiring rules that govern how they integrate input signals, transform them, and communicate them to other regions are poorly understood. Thus, scalable methods for measuring the synaptic connectivity motifs through which different cell types connect are sorely needed. We demonstrate an all-optical approach for measuring the presence and strength of long-range synaptic connections onto single neurons that integrates optogenetic

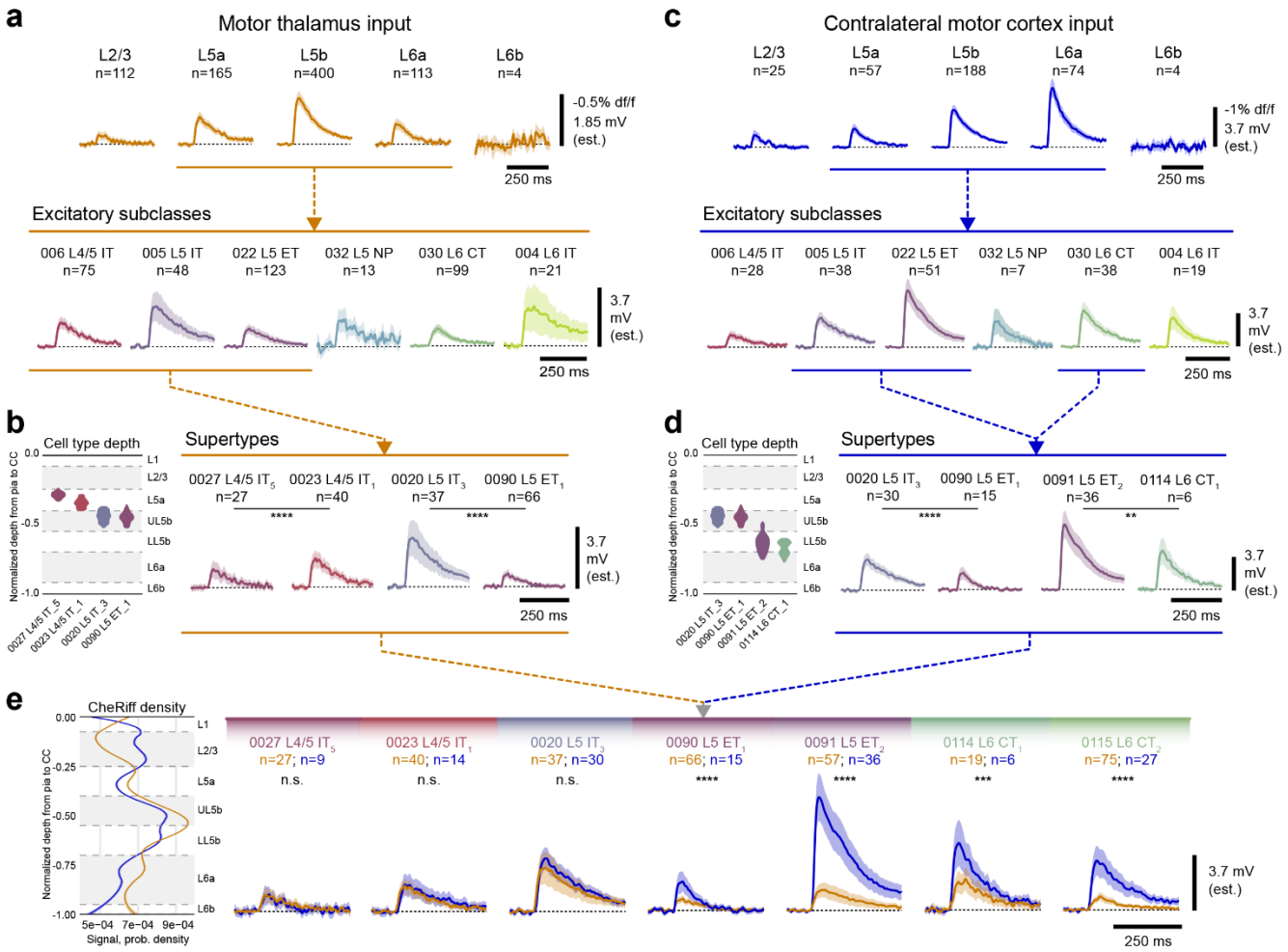

Figure 5 – OCM-FISH data provide cell type-specific insights into long-range circuit connectivity. (***a***) Motor cortex PSPs resulting from activation of MThal inputs, grouped across all cell types by laminar depth (top), and across excitatory cell types by cell subclass for excitatory cells found in L5a-6a (bottom). Line shows mean PSP trace, shaded area shows SEM. (***b***) Laminar position of the four most abundant excitatory supertypes in the 006 L4/5 IT, 005 L5 IT, and 022 L5 ET subclasses localized to L5a and upper L5b (left), alongside average PSPs for each supertype (right; *** = $p < 0.001$, **** = $p < 0.0001$ by two-tailed t-test). (***c***) Motor cortex PSPs resulting from activation of contra motor cortex inputs, grouped across all cell types by laminar depth (top), and across excitatory cell types by cell subclass for cells found in L5a-6a (bottom). (***d***) Laminar position of the 0020 L5 IT_3, 0090 L5 ET_1, 0091 L5 ET_2, and 0114 L6 CT_1 supertypes (left), alongside average PSPs for each supertype (right; **** = $p < 0.0001$, ** = p 0.001). (***e***) Probability density distributions (left) of CheRiff-EGFP signal across all OCM-FISH imaged sections in the MThal-to-motor cortex circuit (orange), and the Contra-to-motor cortex circuit (blue; line shows mean, shaded area shows 95% CI), alongside average PSPs of cell supertypes shown in b and d, colored based on activated pathway (MThal in orange, Contra in blue; line shows mean PSP trace, shaded area shows SEM; **** = $p < 0.0001$; n.s. = not significant).

248 control of presynaptic cells and optical detection of postsynaptic potentials (PSPs) with voltage imaging.
249 This approach for optical circuit mapping (OCM) is sensitive, highly parallelizable, and can be readily
250 combined with fluorescence in situ hybridization (FISH) for cell type identification. Combining each of
251 these components into an integrated platform (OCM-FISH), we assayed the strength of contralateral and
252 thalamic synaptic input onto more than 1,000 transcriptomically identified neurons in the mouse motor
253 cortex, allowing us to expand our understanding of cortical architecture.

254 Previous work examining the specificity of connections to a subset of broadly defined cell types has
255 suggested that long-range inputs target different cortical lamina. For instance, CRACM experiments have
256 suggested that long-range inputs from the MThal strongly innervate pyramidal cells in L5a and 5b of the
257 vibrissal primary motor cortex[33], and strongly innervate IT cells in L5b and L6a of motor cortex[34]. However,
258 there exists a large diversity of cell types within individual cortical lamina, and within broadly defined
259 types. Existing methods lack the throughput to assay the probability and strength of long-range connectivity
260 onto many cells and cell types. Using OCM-FISH, we found that MThal axons more strongly target specific
261 IT cell types in L5a, and that the dominant IT cell type in upper layer 5b is targeted much more strongly
262 than intermingled ET cells (**Fig. 5b**). Past work suggested that input from the MThal to the motor cortex
263 weakly drives corticothalamic (CT) neurons in L6a[29,33,34]. We also found that L6a CT neurons were weakly
264 driven by MThal axon activation, particularly compared to neighboring L6 IT neurons (**Fig. 5a**), but our
265 ability to sample large numbers of cells revealed a superficial L6 CT cell type that was driven strongly, in
266 contrast to the more prevalent L6 CT supertype found in deeper L6a (**Fig. 5e**).

267 Corticocortical input from ipsilateral secondary motor cortex to primary motor cortex has been shown to
268 innervate the deepest cortical layers (L5b and 6a) most strongly[33]. Interestingly, OCM-FISH revealed
269 similar broad connectivity patterns for contralateral motor cortex input, but again provided a high degree
270 of additional specificity when cell types are delineated precisely. For example, contralateral input
271 powerfully targets the L5 ET_2 type, found in lower L5b, compared to the laminarly adjacent L5 ET_1. MThal
272 input onto ET cells followed the same pattern, notable in the context of past work, which demonstrated that
273 ET_2 neurons – which uniquely project to motor circuits in the medulla and spinal cord – are modulated
274 strongly and with low latency at movement onset compared to L5b ET_1 neurons[32]. That ET_2 neurons receive
275 much stronger long-range drive from multiple sources could represent a potential synapse-level mechanism
276 for the fast modulation of ET_2 dynamics that accompany movements – an intriguing hypothesis that can be
277 examined closer in future work. Together, these data establish both pathway- and cell-type specificity in
278 how neurons integrate long-range inputs. Evaluating the molecular code that establishes how particular
279 presynaptic populations selectively innervate transcriptomically distinct postsynaptic neurons will be
280 another exciting future direction.

281 Large-scale mapping of synaptic connections using optical strategies has been previously explored in
282 several ways. For example, 'influence mapping' combines presynaptic optogenetic activation with
283 postsynaptic calcium imaging to uncover both the electrophysiological and functional contributions of
284 individual cells in a circuit[35,36]. However, because calcium imaging cannot report subthreshold activity in
285 neurons, it is difficult to make direct inferences about monosynaptic connectivity between neurons using
286 this strategy. Whether the sensitivity of this approach is sufficient to detect the large majority of connections
287 is also unclear. Voltage-Seq also combines optogenetic activation of presynaptic axonal fibers with voltage
288 imaging, but with the goal of assessing how long-range inputs affect population-level dynamics, including
289 through polysynaptic pathways, rather than reporting direct synaptic connections[37]. Voltage-Seq integrates
290 these measurements with micropipette-based isolation of a subset (~1%) of imaged neurons for RNA-Seq
291 and transcriptomic identification. Thus, this method can describe cell type-specific dynamics in a circuit
292 but does not attempt to identify monosynaptic connectivity motifs. Further, due to its reliance on physical
293 isolation of cells for transcriptomic identification, its scalability is limited compared to OCM-FISH.

294 Despite its advantages, OCM-FISH has several limitations. PSPs resulting from synaptic connections onto
295 distal dendrites of postsynaptic neurons may be attenuated at the soma and thus difficult to detect via
296 somatic GEVI imaging (but see [25]). Additionally, some dendritic segments may be severed in brain slices

in vitro, leading to an underestimation of connectivity. Nevertheless, CRACM is limited in largely the same manner and has been an indispensable tool for assessing long-range connectivity since its introduction. In our repetitive photoactivation paradigm, we observed some nonstationarity in PSP amplitude, with PSPs attenuating over time. This attenuation could reflect the invocation of synaptic plasticity, or a reduced capacity of severed axons to repeatedly release neurotransmitter. Importantly, however, the observed nonstationarity was pathway-specific and minimal in the absence of pharmacological agents, suggesting that these explanations may be unlikely. Future work will be needed to better understand and mitigate this issue. For example, optogenetic photoactivation could be applied at much lower repetition rates while withholding imaging during the inter-stimulus intervals to avoid photobleaching. Alternatively, it may also be possible to perform OCM using higher intensity illumination than was applied here along with minimal repetition, but this could invoke a problematic level of photobleaching. Finally, one cannot ensure that all Voltron2+ cells are viable during OCM *in vitro*, another potential source of false negative connections. Notably, no mRNA was detectable in some (15-20%) Voltron2+ cells, particularly near the cut surface of tissue sections where cell damage is most acute, likely an indication of damaged cells. Excluding Voltron2+ neurons lacking mRNA of the normally highly expressed *Snap25* gene may have mitigated this potential concern.

Importantly, the scalability and sensitivity with which synaptic connections can be assayed, and the resolution with which cell types can be classified are not constrained by any fundamental limits here. Thus there exists opportunity to improve OCM-FISH along each of these axes in future work. We assayed connectivity onto hundreds of neurons per experiment, requiring only a few minutes of OCM imaging per FOV. This could be increased further – perhaps by an additional order of magnitude to include thousands of cells – through future optimization. The per-experiment throughput of OCM-FISH is principally determined by the volume over which the GEVI is expressed and the density of expression across that area. Here, the region of GEVI expression was substantially smaller than the size of the terminal zone of long-range axons, as GEVI expression was achieved using spatially localized intracranial virus injection. GEVI expression over a larger spatial extent using alternative transgenic or viral approaches would permit connectivity measurements in cells occupying a larger spatial region. In addition, sparse (2-5% of cells) GEVI expression allowed us to use simple, widefield microscopy for voltage imaging while minimizing out-of-focus fluorescence and optical crosstalk between cells. Although the simplicity of this approach is a feature, utilizing more advanced fast, light-efficient imaging methods that provide optical sectioning, such as TICO microscopy[38], would permit low-background, low-crosstalk GEVI imaging at substantially higher labeling densities and commensurately higher throughput.

By averaging across repeated synaptic events, we estimated that millivolt-scale PSPs should be detectable here in most neurons, with the sensitivity threshold of PSP detection typically on the order of a 0.5 mV (**Fig. 1g**). Because of the linearity of the fluorescence-voltage (F-V) relationship of Voltron2 in the subthreshold regime[25], sensitivity can be increased by increasing signal (the slope of the F-V relationship) or reducing noise. Noise can be minimized by reducing background fluorescence (e.g. using confocal voltage imaging), increasing the photon collection rate, and/or increasing the number of postsynaptic events averaged. Together, these optimizations could reduce the PSP detection threshold further by several fold.

Optimization of sensitivity in this way may permit unitary synaptic potentials (typically 0.1 to 2.5 mV in amplitude in the cortex[39–41]) to be detected reliably with OCM. In combination with single-neuron optogenetic photoactivation, this would provide a method for detecting pairwise connections between single neurons in a massively parallel manner. In "Optomapping", optogenetic activation is used to serially activate individual presynaptic neurons while PSPs are detected in a single postsynaptic neuron with patch-clamp electrophysiology[42]. This approach allows N potential connections to be investigated in each experiment, where N is the number of presynaptic neurons that can be targeted presynaptically. Combining optogenetic photoactivation and optical detection of PSPs in each of the N neurons would increase local connectivity mapping throughput from N (tens to hundreds) to N^2 (hundreds to tens of thousands) cell-pairs at a time. Without combinatorial expression of these constructs, the current implementation of OCM-FISH

could be used to evaluate local connectivity by limiting opsin expression to a defined population of cells within a local circuit using transgenic animals or enhancer AAVs[43], rather than a distal source region. Only a single presynaptic population could be targeted in each experiment, but the connectivity of those neurons could be assayed onto many nearby cells and cell types simultaneously using the same approach.

Finally, OCM can be combined with myriad techniques for spatial transcriptomics and cell type identification. High-plex spatial transcriptomics methods now provide a means for discerning cell types with higher resolution than we present here[44], although this remains challenging to scale across multiple tissue sections and experiments. OCM-FISH has the potential to be a powerful tool for identifying cell-type specific connectivity motifs across many circuits in the brain, and offers an opportunity to efficiently characterize how cell-type specific connectivity patterns change dynamically as a function of learning or disease.

Acknowledgements

We thank A. Abdelfattah and J. Mertz for advice and discussions, and the Boston University Micro/Nano Imaging Facility for providing technical resources. We additionally thank A.M. Zambon for assistance in the lab, and J. Chen, T. Wang, and N. Li for comments on the manuscript. This work was supported by research grants from the National Institutes of Health: RF1MH126882 (M.N.E.), F32MH129149 (M.V.M.), and K99NS139312 (M.V.M). The funder had no role in study design, data collection and analysis, decision to publish, or preparation of the manuscript.

Author Contributions

MVM and MNE conceived of the project. MNE supervised research. MVM performed experiments, with assistance from JPV, and with resources provided by TW. MVM and WJC analyzed data. MVM and MNE wrote the paper.

References

1. Marr, D. A theory of cerebellar cortex. *J. Physiol.* **202**, 437–470 (1969).
2. Lorente De Nó, R. Studies on the structure of the cerebral cortex. II. Continuation of the study of the ammonic system. *J. Für Psychol. Neurol.* **46**, 113–177 (1934).
3. Green, J. D. & Adey, W. R. Electrophysiological studies of hippocampal connections and excitability. *Electroencephalogr. Clin. Neurophysiol.* **8**, 245–262 (1956).
4. Albin, R. L., Young, A. B. & Penney, J. B. The functional anatomy of basal ganglia disorders. *Trends Neurosci.* **12**, 366–375 (1989).
5. DeLong, M. R. Primate models of movement disorders of basal ganglia origin. *Trends Neurosci.* **13**, 281–285 (1990).
6. Hubel, D. H. & Wiesel, T. N. Receptive fields, binocular interaction and functional architecture in the cat's visual cortex. *J. Physiol.* **160**, 106 (1962).
7. Hubel, D. H. & Wiesel, T. N. Receptive fields and functional architecture of monkey striate cortex. *J. Physiol.* **195**, 215–243 (1968).
8. Mountcastle, V. B. The columnar organization of the neocortex. *Brain* **120**, 701–722 (1997).
9. Famiglietti, E. V. & Kolb, H. Structural Basis for ON-and OFF-Center Responses in Retinal Ganglion Cells. *Science* **194**, 193–195 (1976).
10. Yao, Z. *et al.* A taxonomy of transcriptomic cell types across the isocortex and hippocampal formation. *Cell* **184**, 3222-3241.e26 (2021).
11. Yao, Z. *et al.* A high-resolution transcriptomic and spatial atlas of cell types in the whole mouse brain. *Nature* **624**, 317–332 (2023).
12. Denk, W. & Horstmann, H. Serial Block-Face Scanning Electron Microscopy to Reconstruct Three-Dimensional Tissue Nanostructure. *PLOS Biol.* **2**, e329 (2004).

13. Helmstaedter, M. *et al.* Connectomic reconstruction of the inner plexiform layer in the mouse retina. *Nature* **500**, 168–174 (2013).
14. MICrONS Consortium. Functional connectomics spanning multiple areas of mouse visual cortex. *Nature* **640**, 435–447 (2025).
15. Zingg, B. *et al.* AAV-Mediated Anterograde Transsynaptic Tagging: Mapping Corticocollicular Input-Defined Neural Pathways for Defense Behaviors. *Neuron* **93**, 33–47 (2017).
16. Zingg, B., Peng, B., Huang, J., Tao, H. W. & Zhang, L. I. Synaptic Specificity and Application of Anterograde Transsynaptic AAV for Probing Neural Circuitry. *J. Neurosci.* **40**, 3250–3267 (2020).
17. Wickersham, I. R. *et al.* Monosynaptic Restriction of Transsynaptic Tracing from Single, Genetically Targeted Neurons. *Neuron* **53**, 639–647 (2007).
18. Jin, L. *et al.* Long-term labeling and imaging of synaptically connected neuronal networks in vivo using double-deletion-mutant rabies viruses. *Nat. Neurosci.* **27**, 373–383 (2024).
19. Perin, R., Berger, T. K. & Markram, H. A synaptic organizing principle for cortical neuronal groups. *Proc. Natl. Acad. Sci.* **108**, 5419–5424 (2011).
20. Jiang, X. *et al.* Principles of connectivity among morphologically defined cell types in adult neocortex. *Science* **350**, aac9462 (2015).
21. Campagnola, L. *et al.* Local connectivity and synaptic dynamics in mouse and human neocortex. *Science* **375**, eabj5861 (2022).
22. Petreanu, L., Huber, D., Sobczyk, A. & Svoboda, K. Channelrhodopsin-2–assisted circuit mapping of long-range callosal projections. *Nat. Neurosci.* **10**, 663–668 (2007).
23. Petreanu, L., Mao, T., Sternson, S. M. & Svoboda, K. The subcellular organization of neocortical excitatory connections. *Nature* **457**, 1142–1145 (2009).
24. Hochbaum, D. R. *et al.* All-optical electrophysiology in mammalian neurons using engineered microbial rhodopsins. *Nat. Methods* **11**, 825–833 (2014).
25. Abdelfattah, A. S. *et al.* Sensitivity optimization of a rhodopsin-based fluorescent voltage indicator. *Neuron* **111**, 1547-1563.e9 (2023).
26. Grimm, J. B. *et al.* A general method to optimize and functionalize red-shifted rhodamine dyes. *Nat. Methods* **17**, 815–821 (2020).
27. Shu, Y., Yu, Y., Yang, J. & McCormick, D. A. Selective control of cortical axonal spikes by a slowly inactivating K+ current. *Proc. Natl. Acad. Sci.* **104**, 11453–11458 (2007).
28. Cruikshank, S. J., Urabe, H., Nurmikko, A. V. & Connors, B. W. Pathway-Specific Feedforward Circuits between Thalamus and Neocortex Revealed by Selective Optical Stimulation of Axons. *Neuron* **65**, 230–245 (2010).
29. Guo, K., Yamawaki, N., Svoboda, K. & Shepherd, G. M. G. Anterolateral Motor Cortex Connects with a Medial Subdivision of Ventromedial Thalamus through Cell Type-Specific Circuits, Forming an Excitatory Thalamo-Cortico-Thalamic Loop via Layer 1 Apical Tuft Dendrites of Layer 5B Pyramidal Tract Type Neurons. *J. Neurosci.* **38**, 8787–8797 (2018).
30. Yang, W., Tipparaju, S. L., Chen, G. & Li, N. Thalamus-driven functional populations in frontal cortex support decision-making. *Nat. Neurosci.* **25**, 1339–1352 (2022).
31. Choi, H. M. T. *et al.* Third-generation in situ hybridization chain reaction: multiplexed, quantitative, sensitive, versatile, robust. *Development* **145**, (2018).
32. Economo, M. N. *et al.* Distinct descending motor cortex pathways and their roles in movement. *Nature* **563**, 79–84 (2018).
33. Hooks, B. M. *et al.* Organization of Cortical and Thalamic Input to Pyramidal Neurons in Mouse Motor Cortex. *J. Neurosci.* **33**, 748–760 (2013).
34. Yamawaki, N. & Shepherd, G. M. G. Synaptic circuit organization of motor corticothalamic neurons. *J. Neurosci. Off. J. Soc. Neurosci.* **35**, (2015).
35. Chettih, S. N. & Harvey, C. D. Single-neuron perturbations reveal feature-specific competition in V1. *Nature* **567**, 334–340 (2019).
36. Bounds, H. A. & Adesnik, H. Network influence determines the impact of cortical ensembles on stimulus detection. *Neuron* **0**, (2025).

37. Csillag, V., Bizzozzero, M. H., Noble, J. C., Reinius, B. & Fuzik, J. Voltage-Seq: all-optical postsynaptic connectome-guided single-cell transcriptomics. *Nat. Methods* **20**, 1409–1416 (2023).
38. Xiao, S. *et al.* Large-scale deep tissue voltage imaging with targeted-illumination confocal microscopy. *Nat. Methods* **21**, 1094–1102 (2024).
39. Markram, H., Lübke, J., Frotscher, M., Roth, A. & Sakmann, B. Physiology and anatomy of synaptic connections between thick tufted pyramidal neurones in the developing rat neocortex. *J. Physiol.* **500**, 409–440 (1997).
40. Song, S., Sjöström, P. J., Reigl, M., Nelson, S. & Chklovskii, D. B. Highly Nonrandom Features of Synaptic Connectivity in Local Cortical Circuits. *PLOS Biol.* **3**, e68 (2005).
41. Jiang, X. *et al.* Principles of connectivity among morphologically defined cell types in adult neocortex. *Science* **350**, aac9462 (2015).
42. Chou, C. Y. C. *et al.* Principles of visual cortex excitatory microcircuit organization. *The Innovation* **6**, 100735 (2025).
43. Ben-Simon, Y. *et al.* A suite of enhancer AAVs and transgenic mouse lines for genetic access to cortical cell types. *Cell* **188**, 3045-3064.e23 (2025).
44. Fang, R. *et al.* Three-dimensional single-cell transcriptome imaging of thick tissues. *eLife* **12**, (2024).
45. Ting, J. T. *et al.* Preparation of Acute Brain Slices Using an Optimized N-Methyl-D-glucamine Protective Recovery Method. *JoVE J. Vis. Exp.* e53825 (2018) doi:10.3791/53825.
46. Wang, Y. *et al.* EASI-FISH for thick tissue defines lateral hypothalamus spatio-molecular organization. *Cell* **184**, 6361-6377.e24 (2021).
47. Lubeck, E., Coskun, A. F., Zhiyentayev, T., Ahmad, M. & Cai, L. Single-cell in situ RNA profiling by sequential hybridization. *Nat. Methods* **11**, 360–361 (2014).
48. Schindelin, J. *et al.* Fiji: an open-source platform for biological-image analysis. *Nat. Methods* **9**, 676–682 (2012).
49. Pachitariu, M. & Stringer, C. Cellpose 2.0: how to train your own model. *Nat. Methods* **19**, 1634–1641 (2022).
50. Stringer, C. & Pachitariu, M. Cellpose3: one-click image restoration for improved cellular segmentation. *Nat. Methods* **22**, 592–599 (2025).
51. Klein, S., Staring, M., Murphy, K., Viergever, M. A. & Pluim, J. P. W. elastix: A Toolbox for Intensity-Based Medical Image Registration. *IEEE Trans. Med. Imaging* **29**, 196–205 (2010).
52. Berg, S. *et al.* ilastik: interactive machine learning for (bio)image analysis. *Nat. Methods* **16**, 1226–1232 (2019).
53. Pnevmatikakis, E. A. & Giovannucci, A. NoRMCorre: An online algorithm for piecewise rigid motion correction of calcium imaging data. *J. Neurosci. Methods* **291**, 83–94 (2017).

MATERIALS AND METHODS

Animals

All animal procedures and experiments were performed with approval from the Boston University Institutional Animal Care and Use Committee (IACUC) and in compliance with policies and guidelines from the National Institutes of Health (NIH). Both male and female C57BL/6J mice (JAX #000664) were used for all experiments described. Mice were housed on a 12-h light/dark cycle at 21 ± 3°C and 30–70% humidity with ad libitum access to food and water.

Experimental Procedures

Virus injections

Virus was injected into animals between 5-7 weeks of age. Anesthesia was induced using 4% isoflurane until animal was unresponsive to toe pinch. Animals were then maintained under anesthesia using a constant

flow of 0.8% isoflurane through a nose cone in the stereotaxic apparatus. Saline ointment was applied to both eyes, and pre-operative Ketoprofen (4 mg/kg, 1 mg/mL solution in sterile saline) and Buprenorphine HCl (0.072 mg/kg, 0.03 mg/mL solution in sterile saline) analgesics were delivered via subcutaneous injection (S.C.). Bupivacaine HCl (100 µL of a 5 mg/mL solution in sterile saline) was delivered subcutaneously to numb the scalp and periosteum. Nair hair removal cream was applied to the scalp to remove fur. Betadine was then topically applied and the scalp and periosteum were resected to expose the skull. Exposed scalp margins were secured to the skull with cyanoacrylate glue. The animal's head was oriented to bring the bregma and lambda sutures to the same z-depth, and to ensure the bilateral parietal skull plates were leveled. Craniotomies were then made over target regions of the brain, leaving only a thin layer of bone that could be punctured by a beveled pipette. To express CheRiff-EGFP in presynaptic neurons, 50 nL of a sterile PBS solution containing AAV9-hSyn-CheRiff-EGFP virus (titer of 1.0E12 g.c.) was delivered via glass pipette to motor thalamus (MThal) at -1.6 mm AP, +0.8 mm ML, -4.25 mm (VM of MThal) and -1.0 mm AP, +1.3 mm ML, -3.6 mm DV (VAL of MThal; coordinates from bregma), or to contralateral motor cortex (Contra) at 6 different AP/ML sites located at +0.7/1.3/1.9 mm AP, -1.9/1.5 mm ML, -1.0 mm and -0.5 mm DV. In ipsilateral motor cortex, 50 nL of sterile PBS solution containing AAV1-hSyn-FLEX-Voltron2 (titer of 1.0E12 g.c.) mixed with AAVretro-hSyn-Cre or AAV5-hSyn-Cre (titer of 0.5-1.0E11 g.c.) was delivered to two depths at 3 different AP sites: +0.7/1.3/1.9 mm AP, +1.7 mm ML, -1.0 mm and -0.5 mm DV. Virus solutions were delivered at a rate of about 1 nL/sec using a Narishige microvolume ejector. The skull of the animal was then covered with dental cement to cover surgical areas. Animals were given postoperative Ketoprofen once per day for the following two days.

Acute slicing

Acute slices were made using an N-methyl-D-glucamine (NMDG)-based protective recovery method[45]. Briefly, animals were perfused with 15 mL chilled and carbogen-bubbled (95% O_2/5% CO_2) NMDG-HEPES aCSF (in mM: 92 NMDG, 2.5 KCl, 1.25 $NaH_2PO4 \bullet 2H_2O$, 30 $NaHCO_3$, 20 HEPES, 25 D-Glucose, 2 Thiourea, 5 (+)-Na-L-ascorbate, 3 Na-pyruvate, 0.5 $CaCl_2 \bullet 4H_2O$, 10 $MgSO_4 \bullet 7H_2O$, pH adjusted to 7.3-7.4 with HCl) at 10 mL/min. The brain was then rapidly dissected in chilled and bubbled NMDG-HEPES aCSF and mounted for vibratome sectioning. 300 µm slices were made in a para-coronal plane (with anterior tissues oriented slightly ventrally) through motor cortex with chilled and bubbled NMDG-HEPES in the bath. Additional acute slices were collected through MThal injection sites if present, immediately fixed in fresh 4% paraformaldehyde in PBS for 30 min, and stored at 4°C in PBS. motor cortex slices were immediately moved to a chamber with 34°C bubbled NMDG-HEPES, where NaCl was reintroduced gradually via periodic spike-ins of 2M NaCl in NMDG-HEPES at 5 min. intervals. Slices were then incubated for 1 hour in a small chamber containing 25 nmol of JF585 dye in room temperature, bubbled HEPES aCSF (in mM: 92 NaCl, 2.5 KCl, 1.25 $NaH_2PO_4 \bullet 2H_2O$, 30 $NaHCO_3$, 20 HEPES, 25 D-Glucose, 2 Thiourea, 5 (+)-Na-L-ascorbate, 3 Na-pyruvate, 2 $CaCl_2 \bullet 4H_2O$, 2 $MgSO_4 \bullet 7H_2O$, pH adjusted to 7.3-7.4 with NaOH). Finally, slices were transferred to a chamber containing room temperature, bubbled HEPES aCSF, where they were held until imaging. Imaging experiments were performed in either the above HEPES aCSF or in recording aCSF (in mM: 124 NaCl, 2.5 KCl, 1.2 $NaH_2PO_4 \bullet 2H_2O$, 24 $NaHCO_3$, 5 HEPES, 12.5 D-Glucose, 2 $CaCl_2 \bullet 4H_2O$, 2 $MgSO_4 \bullet 7H2O$, pH adjusted to 7.3-7.4 with NaOH). OCM experiments were performed with 200nM-1µM TTX and 100 µM 4-AP (Tocris #1069 and #0940) in the extracellular recording aCSF. For experiments including glutamatergic blockers, 10 µM NBQX and 10 µM D-AP5 (Tocris #1044 and #0106) were applied to the extracellular recording aCSF.

Whole-cell patch clamp

For whole-cell recording experiments, fire-polished, filamented glass pipettes (1.5 mm OD, 0.86 mm ID, #BF150-86-10 Sutter Instruments) were pulled to 3-7 MΩ resistance using a P-1000 horizontal micropipette puller (Sutter Instruments). Pipettes were loaded with an internal solution containing (in mM) 130 K-gluconate, 4 KCl, 10 HEPES, 0.3 EGTA, 10 Phosphocreatine-Na_2, 4 MgATP, and 0.3 Na_2GTP. Cells were visualized using oblique illumination with an M660L4 LED (ThorLabs) through a condenser focused through the glass of the bath onto the sample to produce a DIC-like image. An Axon Instruments

MultiClamp 700b amplifier and patch-clamp headstage (Molecular Devices #1-CV-7B) mounted on a motorized four-axis Siskiyou MX7600 manipulator were used to acquire all electrophysiology data.

Voltage imaging and optogenetic photoactivation

During voltage imaging, slices were continually perfused with room temperature, bubbled HEPES aCSF via peristaltic pump. OCM experiments were performed with 200 nM-1 µM TTX and 100 µM 4-AP added to the perfused aCSF. Widefield images were acquired using a Nikon 16X/0.8NA water-immersion objective (#CFI75 LWD 16X W) or an Olympus 20X/1.0NA water-immersion objective (#N20X-PFH). To illuminate the sample, a M565L3 LED (Thorlabs) was used with an ET 577/25x excitation filter, T590lpxr dichroic beam splitter, and an ET 590lp emission filter (Chroma). A 300mm 200 EFL lens (Edmund optics) was used to focus the signal onto the sensor of an ORCA-Flash4.0 v3 CMOS (Hamamatsu, model #C13440-20CU) or a Kinetix sCMOS (Teledyne Vision Solutions, model #01-KINETIX-M-C). For optogenetic photoactivation, an M470L4 LED was used. During OCM experiments, LEDs and camera acquisition was triggered using digital waveforms generated in Wavesurfer (https://wavesurfer.janelia.org/) via a digital-to-analog converter (National Instruments #BNC 2090), and LED Drivers (Thorlabs #LEDD1B). The 565nm imaging LED was used for all acquisitions (2.7-11mW). For patch experiments, the 470nm opto stim LED was pointed obliquely at the sample, and used at powers ranging from 18 to 66 µW (corresponding to 0.5 to 5.0 ms trigger pulse widths respectively). For OCM experiments, the opto stim LED was used at 50 µW (1.0 ms trigger pulse width) and placed below the sample, with light focused onto the sample through a condenser. Opto stim was performed at 2 or 4 Hz for patch clamp experiments and 2 Hz for OCM experiments, while continuously acquiring Voltron2-JF585 fluorescence signal at 400 Hz. For patch clamp experiments, either a 128 x 128 pixel or 1024 x 256 pixel field-of-view (FOV) with a 2x binning factor was used to acquire data. For OCM experiments, variable FOV sizes were used, aiming to image as many cells per section as possible while maintaining a 400 Hz imaging rate. After completion of OCM, imaged sections were incubated in RNase-Free 4% paraformaldehyde in PBS for 30-45 minutes at room temperature (RT) with gentle agitation, then stored in PBS at 4°C.

Pre-HCR mFISH histology

OCM sections were microdissected to remove all but the dorsal cortical region containing Voltron2-positive neurons in motor cortex, then incubated for 1.5-2 hrs at RT in a dye mixture containing 1:1000 NeuroTrace 435/455 and 1:100 SYTO 45 dye (Thermo Fisher #N21479 and #S11350 respectively) in PBS to label nucleic acids in all neurons in the sample. motor cortex sections were briefly washed and mounted in 85% 2,2'-thiodiethanol (TDE) in ultra-pure water, ensuring that the OCM-imaged slice face was face up on the slide. NeuroTrace/SYTO, CheRiff-EGFP, and Voltron2-JF585 fluorescence was imaged on a Nikon CSU-W1 SoRa spinning disk confocal microscope. 40X image stacks with 2 µm spacing through 50-80 µm of axial z-depth were collected, with enough XY tiled sampling to visualize all Voltron2-positive neurons in each section. Sections were removed from the slide and washed for 15 min in PBS at RT before proceeding to our custom HCR mFISH protocol.

Adapted multi-round HCR mFISH protocol for thick tissue

Multiplexed FISH was performed using an adapted version of the Molecular Instruments HCRv3 "generic sample in solution" protocol[31], incorporating multi-round probing and stripping[46,47].

All chemical reagents were not used for more than 2 months after opening, and all solutions were prepared using nuclease free stocks, salts, water. RNaseZap (Thermo Fisher #AM9780) or RNase AWAY (Thermo Fisher #7002) was used to clean all instruments used during the HCR procedure. Unless otherwise stated, all washes and incubations were performed with end-over-end rotation in 600 µL microcentrifuge tubes, using 200 µL of solution per slice and per tube. Day 0: After pre-HCR imaging, OCM samples were incubated in 90% DMSO in PBS at RT for 2 hours. After 1 brief rinse in PBS, slices were each moved to a well of a 12-well plate containing freshly prepared 1% $NaBH_4$ in PBS and incubated at RT for 15 minutes on an orbital shaker. Slices were carefully transferred back to a new microcentrifuge tube containing PBS and washed 3 x 5 min at RT to remove all $NaBH_4$ solution. Slices were stored in fresh PBS at 4°C until the

following day. Day 1: PBS from the sample tubes was exchanged for 8% SDS in PBS (prepared fresh from a 10% SDS stock in water) and slices were incubated for 4 hours at RT. Excess SDS was removed by washing the slices 3 x 5 min and then 3 x 1 hr in PBS at RT. From this point, the Molecular Instruments HCRv3 protocol for staining a "generic sample in solution" was followed, using the reaction volumes listed above. Briefly, slices were pre-incubated in Hybridization buffer (Molecular Instruments) for 30 min at 37°C. An initiator probe solution containing a final concentration of 4 nM of each initiator probe set (ie., 4 nM per gene of interest) was made in Hybridization buffer. The pre-incubation solution was then exchanged for this initiator probe solution and samples were incubated overnight (ON) at 37°C. Day 2: Wash buffer (Molecular Instruments) was pre-warmed to 37°C by placing into the incubator for approximately 15 minutes before using. Slices were washed in warmed Wash buffer 2 x 15 min and then 2 x 30 min at 37°C. Slices were then washed in 5X SSC with 0.1% Tween20 (5X SSCT) 3 x 5 min at RT, and then stored at 4°C until the end of the day. To end the day, samples were pre-incubated in Amplification buffer (Molecular instruments) for 30 min at RT. During this time, each set of amplifiers needed (per 200 µL reaction volume, 2 µL of h1 and 2 µL of h2 were used per amplifier pair) was melted separately by heating to 95°C for 90 sec and then cooled to room-temperature by 5° per minute in a thermocycler. Amplifiers were spun down and then pooled in fresh Amplification buffer. The pre-incubation solution was then exchanged for the amplifier solution and slices were incubated ON at RT, protected from light. Day 3: Samples were washed 3 x 5 min in 5X SSC (no Tween20) and then incubated in 85% TDE in water to clear before mounting. Slices were carefully moved from the tube to a glass slide and coverslipped in sufficient 85% TDE to cover the samples. Slices were imaged on an Olympus FV3000 laser scanning or Nikon CSU-W1 SoRa spinning disk confocal microscope. 20X or 40X image stacks with 2 µm spacing through 50-80 µm of axial z-depth were collected, with enough XY tiled sampling to visualize the full area of motor cortex that contained Voltron2-positive neurons in each section. Following imaging, the coverglass was removed from the slide, slices were rehydrated with 2X SSC and carefully lifted from the glass with a brush. Samples were placed back into fresh microcentrifuge tubes containing 2X SSC buffer and washed 3 x 5 min in 2X SSC to remove excess TDE. Slices were then pre-incubated in 1X DNaseI buffer (New England Biolabs #B0303) at 37°C for 15 min before being incubated in 1:50 DNaseI (enzyme stock of 2000 U/mL, New England Biolabs #M0303; working concentration of 8 U per 200 µL reaction volume) in 1X DNaseI buffer for 1 hr at 37°C. This solution was then exchanged for a fresh solution of 1:50 DNaseI in 1X DNaseI buffer, and slices were incubated ON at 37°C. Day 4: Samples were incubated in 65% formamide in 2X SSC for 30 min at 37°C. After 2 brief rinses in 2X SSC, each slice was then carefully transferred to a well of a clean well-plate containing freshly prepared 1% $NaBH_4$ in PBS, and incubated for 15 min at RT on an orbital shaker. Slices were then moved back to a clean microcentrifuge tube containing PBS, and washed 3 x 5 min in PBS at RT. Slices were then stored in PBS at 4°C until the end of the day, when the second round of initiator probe hybridization was performed, as described for the end of Day 1. From here, steps repeat as described above until 4-5 rounds of HCR have been performed.

Data Analysis

<u>Voltage imaging sensitivity evaluation using whole-cell patch data</u>

Timeseries data from both whole-cell recording and voltage imaging were segmented in time to isolate each photoactivation /PSP instance, including a post-response baseline period (where cell was at resting). To determine sensitivity of increasing the number of trials averaged (N_t), the z-score of the response amplitude (or response SNR) for an N_t-averaged trace was calculated relative to the distribution of bootstrap-sampled (n = 500) averages of the baseline period in the averaged trace. This comparison was performed 50 times for N_t randomly sampled PSPs in the photoactivation series, and the mean of the 50 resulting SNR measurements was used to determine sensitivity.

650 Evaluation of optimal trial number to average per cell
651 Because some cells in our OCM-FISH experiments showed non-stationarity in PSP amplitude over the
652 course of the photoactivation series, to generate the trial-averaged PSP for each cell, we first determined
653 the optimal number of consecutive PSPs to average (N_o). As above, we first determined the z-score of the
654 response amplitude (or response SNR) for consecutively averaged PSP trials (N_t) relative to the mean and
655 SEM of the baseline period (when cell was at resting) in the averaged trace. The N_o trials to average was
656 taken as the N_t that yielded the largest magnitude SNR response. We additionally bootstrap-sampled (n =
657 500) from the baseline period of the N_t-averaged trace to generate "false PSPs" that could be used to
658 quantify the false-positive rate when using a given SNR threshold for determining whether a cell was
659 "responding" or "not responding". A SNR threshold of $z = -3.75$ yielded a < 0.07 false positive rate across
660 all imaged cells, thus a cell was only considered "responding" if the response amplitude of the N_o-averaged
661 response had an SNR of ≤ -3.75.
662
663 mFISH image segmentation
664 To create individual cell ROIs in initial HCR mFISH runs, the AlexaFluor 488 (AF488) HCR channel
665 containing signal from *Snap25* transcripts was used for segmentation. For OCM-FISH samples, the
666 AlexaFluor 514 (AF514) HCR channel containing signal for *Vip* transcripts and spectral bleed from AF488
667 *Snap25* signal was used for segmentation because a subset of *Vip+* cells did not show *Snap25* expression.
668 The *Vip+Snap25* image was first background-subtracted in FIJI[48] using a rolling ball algorithm with 50-
669 100 px radius and segmented using Cellpose2 or Cellpose3[49,50], with z-axis segmentation performed using
670 the intersection-over-union evaluation with a 70% threshold. Flow threshold and cell probability thresholds
671 were kept at default values (0.4, 0.0 respectively), as were lower and upper pixel intensity percentiles (1.0,
672 99.0 respectively). The pixel value assigned to each cell's ROI was used as the cell ID for all downstream
673 voltage imaging and mFISH classification analyses.
674
675 Multi-round HCR image registration
676 Images of NeuroTrace 435/455 or *Snap25* mFISH signal were used for registering pre-HCR confocal
677 images and HCR mFISH images across imaging rounds. Raw images were first preprocessed to enhance
678 local contrast and remove background signal. Local intensity normalization was applied using a block-
679 based contrast stretching algorithm, followed by background subtraction using a rolling ball algorithm with
680 a 40-pixel radius. Prior to automated registration, an initial affine transformation was estimated from
681 manually selected corresponding landmarks in the fixed and moving images and used to compute an initial
682 affine transform. This transform provided a coarse alignment to facilitate subsequent intensity-based
683 gradient descent. These corresponding points were further used as a metric in the automated gradient
684 descent. Image registration was performed using the elastix software package[51] and was comprised of
685 multiple steps: 1) Affine refinement: an affine transform was optimized combining mutual information
686 between intensities and a corresponding-points Euclidean distance metric. 2) Nonrigid B-spline registration
687 with penalties: a penalized B-spline deformation was applied using 4 resolutions depending on the dataset,
688 optimizing mutual information alongside bending energy and point correspondence penalties. 3) Final
689 nonrigid B-spline refinement: a final non-penalized B-spline registration stage was performed to fine-tune
690 alignment using mutual information alone at the final B-spline resolution.
691
692 Binary annotation of mFISH data and mFISH cell type classification
693 In HCR mFISH experiments used evaluate cell type classification, segmented cell ROIs from full HCR
694 mFISH volumes were annotated in a binary fashion for each gene, such that each cell received a "positive"
695 or "negative" label for each marker gene that was probed. This annotation was performed using the "Object
696 Classification" module in Ilastik[52], which allowed the user to select examples of "positive" and "negative"
697 cells in the sample to train a random forest classifier. This classifier was then applied to annotate the
698 remaining population of segmented neurons in the tissue volume. In OCM-FISH experiments, binary
699 annotation of gene expression was performed on a per-cell and per-gene basis. Briefly, using a custom GUI,
700 the full image volume containing a cell's HCR mFISH signal was evaluated against the shape of the

segmentation ROI and against the Voltron2-JF585 signal (to avoid incorrectly annotating immediately adjacent cells). For a given gene, a "positive" or "negative" label was empirically assigned to each cell. To facilitate evaluation, cells across the tissue volume of interest were ordered based on the ratio of the mean intensity of mFISH signal inside vs. immediately surrounding the cell's ROI. This provided a framework for "batch" annotating subsets of cells in the tissue. A binary annotation matrix for HCR cells (structured as cells x genes) was generated from either Ilastik or manual annotation data. To create comparable binary expression patterns in ABC Atlas scRNA-Seq data[11], we generated a population of "meta cells": cells from the scRNA-Seq dataset whose normalized counts values were summed with those of their 9 nearest neighbors in PCA space (30 PCs). This population of meta cells showed clear multimodal distributions of normalized counts for each gene, composed of low- and high-expressing cells. To draw binarization boundaries between these portions of the distributions, we fit a gaussian mixture model to the distributions (excluding the peak representing zero counts), using the minimum number of gaussians above which decreasing Akaike and Bayes information criteria (AIC/BIC) scores leveled off. We then determined the intersection points between fit gaussians and used these points as thresholds for binarization. For distributions with more than two fit gaussians, the intersection point used was selected such that the data would be divided approximately in half by the threshold. Cells with normalized counts values above the intersection point were considered "positive" for a gene, with cells below labeled as "negative". For each cell type, this allowed us to determine the proportion of cells expressing and not expressing each of the 17 genes probed by HCR. These proportions were used as probabilities in a Bernoulli Bayes Classifier to classify each cell imaged in HCR experiments into a taxonomic cell type. The evaluated cells' depths were used to select depth-specific cell type probabilities (used as the prior probability) derived from ABC MERFISH data, with each cell type having a baseline probability of 0.2% at each depth. The classifier evaluated classification probabilities as follows:

$$P(class|17\ bit\ binary\ pattern) = P(17\ bit\ binary\ pattern|class) * P(class)$$

The classification was performed in a hierarchical fashion, such that the first evaluation was for Glut vs. GABA neurotransmitter type. If a cell was classified as Glut, it would go on to be subclassed into types forming the Glut class. At each evaluation node, the cell type that received the highest probability score became a cell's assigned type. Excitatory neurons were classed down to the level of "supertype", while inhibitory neurons were classed down the "subclass" level.

<u>Columnar CheRiff signal quantification</u>

A maximum intensity projection image of CheRiff-EGFP signal was generated across the z-axis of a confocal CheRiff image. The x-y location of each Voltron2-positive cell from the same confocal volume was then mapped onto this 2D image. A 75 µm-wide column perpendicular to the pial surface and spanning from pia to the corpus callosum, was centered in x around the cell of interest. The mean intensity of CheRiff signal in this column was measured, and a normalized intensity value was generated by normalizing each column's mean to the mean of the brightest column in the same slice. In OCM-FISH data, response amplitudes were normalized to columnar CheRiff intensity by dividing median-normalized response amplitudes (response amplitudes divided by the median amplitude of responding cells in the same slice) by the normalized columnar CheRiff value.

<u>Voltage imaging data registration to HCR confocal data and segmentation masks</u>

To register widefield 2D images of $Voltron2_{JF585}$ signal to 3D confocal volumes of the same signal, the general registration pipeline described for multi-round HCR mFISH image registration was used, with modifications to account for dimensionality. Confocal image stacks were first oriented based on manually selected landmarks and z-projected based on each z-plane correlation with the widefield image. The confocal stacks were additionally Gaussian blurred before running elastix to calculate the final B-spline transform. Finally, Voltron2+ segmentation masks generated from mFISH confocal data were registered to $Voltron2_{JF585}$ widefield images using this same transform, and masks were sub-selected based on alignment to distinguishable cells in the widefield image. These aligned masks were used to extract timeseries data for $Voltron2_{JF585}$ in OCM experiments.

752
753 Timeseries motion correction, background subtraction, and signal extraction
754 Motion correction was performed on widefield timeseries images of Voltron2$_{JF585}$ signal using a modified,
755 GPU-accelerated implementation of the NoRMCorre algorithm1[53]. Rigid registration was applied frame-
756 by-frame using a subpixel-accurate template-matching approach. A representative template was
757 constructed from a batch of 200 frames starting at frame 800 (or the midpoint of the movie, if shorter), and
758 all frames were aligned to this reference using a maximum shift of 15 pixels and an up-sampling factor of
759 50. To correct for large-spatial-scale intensity variations, background was removed using a custom
760 implementation of the rolling ball algorithm, based on the method used in FIJI's Subtract Background
761 plugin[48]. For each frame, a local background estimate was computed by performing a morphological
762 opening on a lightly blurred image with a spherical structuring element of radius larger expected foreground
763 structures. This background was then subtracted from the original frame. Processing was done frame-by-
764 frame to preserve neural activity that varied on faster timescales than the background, ensuring high-
765 frequency signal components were retained. Timeseries data for each cell were extracted as changes in
766 fluorescence over baseline (df/f) using aligned segmentation masks described above.
767

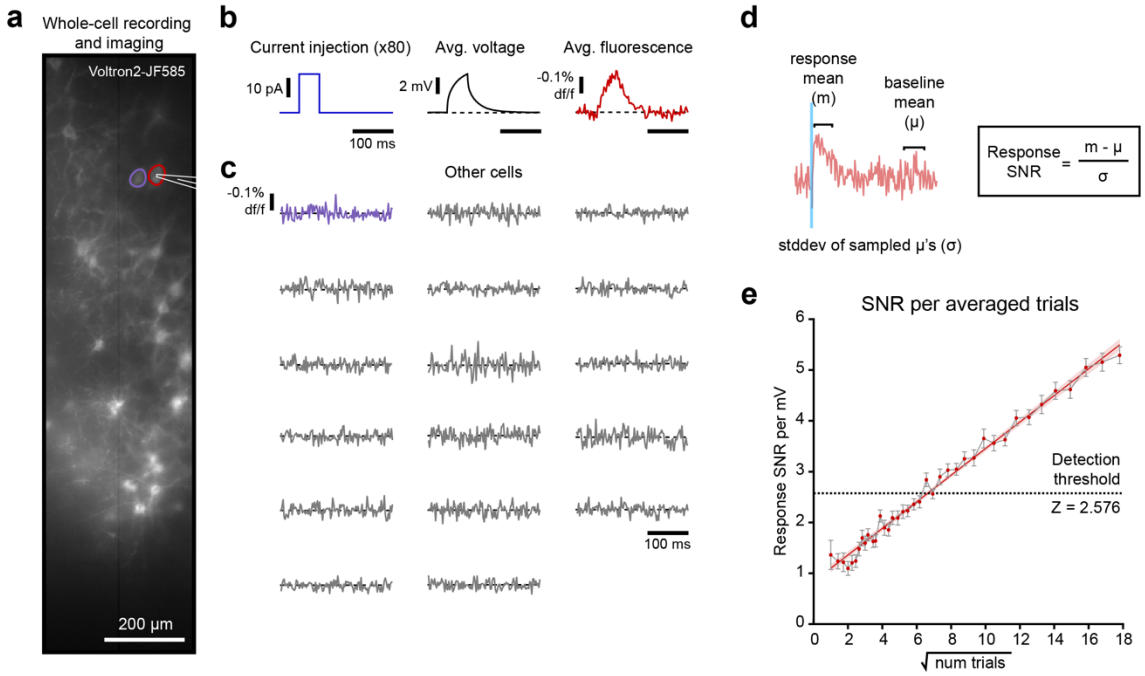

Extended Data Figure 1 – Whole-cell recording with voltage imaging allows for sensitivity measurements. (***a***) Widefield image of Voltron2-JF585-positive cells with two cells highlighted, including a cell that was patched for simultaneous whole-cell recording. (***b***) Short current injections (blue) were performed in patched cells to test for efficacious patch in both membrane voltage recording (black) and voltage imaging data (red). Shown are data from red-highlighted cell in ***a***. (***c***) Voltage imaging timeseries data from other cells in the same field-of-view as cell in ***a*** and ***b***, including an adjacent cell (purple), which did not show changes in fluorescence when patched cell was injected with current. This indicated to spatial cross-talk of signal. (***d***) Schematic example of showing how response signal-to-noise ratios (SNR) were calculated for trial-averaged fluorescence PSP traces using the mean response amplitude (m), the mean baseline signal (µ), and the standard deviation of bootstrap-sampled baseline means (σ). (***e***) Line plot highlighting the linear relationship between response SNR and the square-root of the number of photostimulation trials averaged. A "detectable" response had an SNR of greater than 2.576. Error bars show SEM, and shaded areas around the fit line show 95% CI of fit.

768

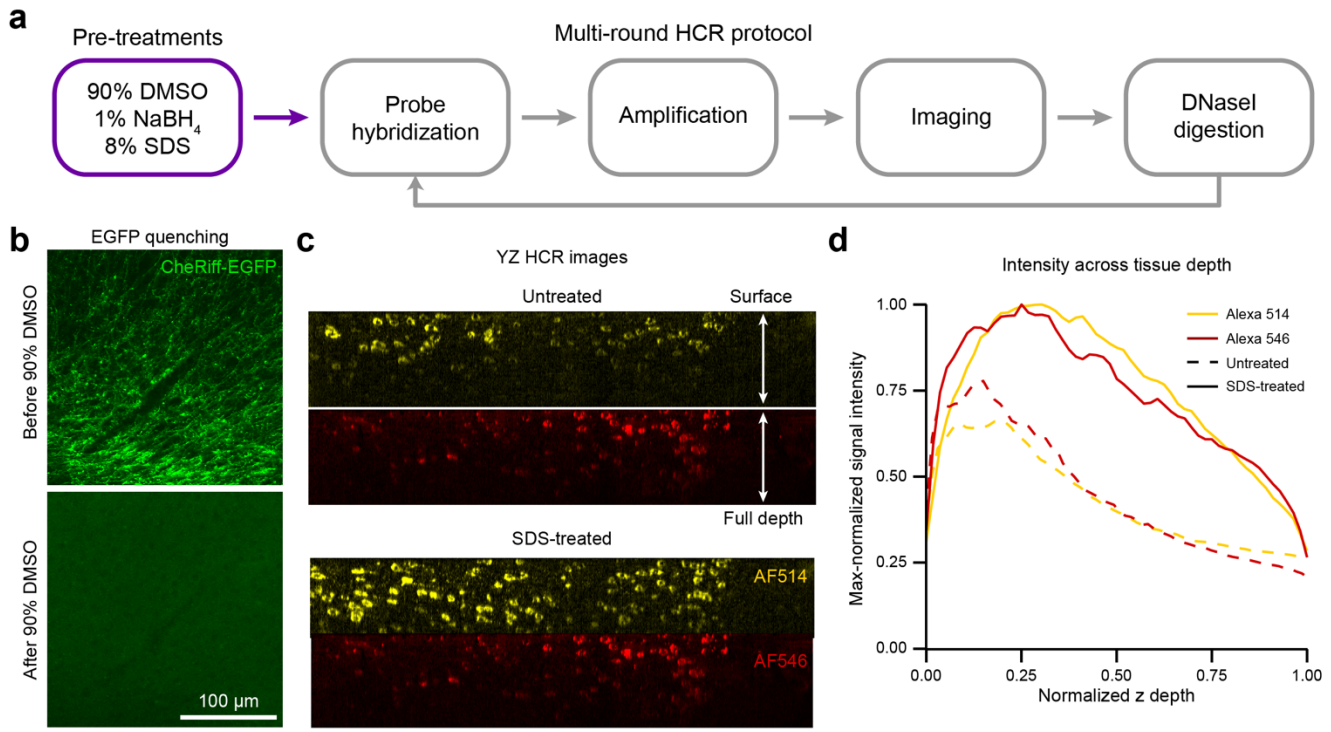

Extended Data Figure 2 – The effect of pre-treatment washes on HCR mFISH in 300 µm-thick tissue samples. (***a***) Outline of custom multi-round HCR mFISH protocol, with pre-treatment steps highlighted in purple. (***b***) Confocal images showing EGFP fluorescence from CheRiff-EGFP fusion before sample incubation in 90% DMSO (top), and absence of EGFP signal following 90% DMSO treatment (bottom). (***c***) Representative orthogonal YZ images through a full-volume confocal z-stack of a 300 µm-thick cortical section. HCR mFISH signal in the AlexaFluor 514 (AF514; yellow) and AF546 (red) channels are shown. Untreated (top) and SDS-treated (bottom) samples are shown. (***d***) Line plots showing quantification of signal intensity across tissue z-depths for AF514 (yellow) and AF546 (red) channels, in both untreated (dotted line) and SDS-treated (solid line) samples.

769

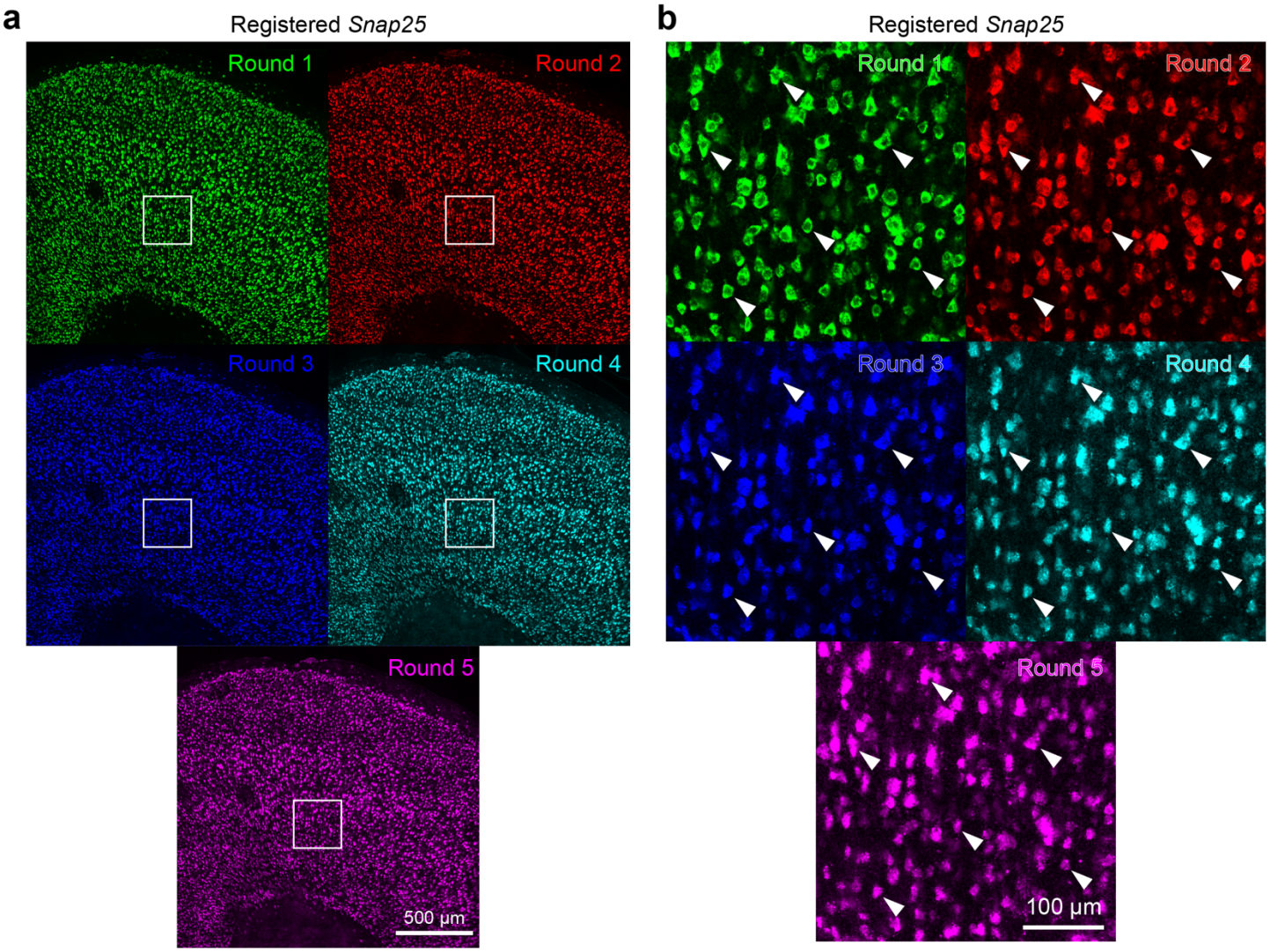

E*xtended Data Figure 3 – Round-to-round registration of mFISH image data using Snap25 signal.* (***a***) Z-projected images of 3 confocal planes, showing registered *Snap25* signal across 5 rounds of HCR mFISH. (***b***) Images from insets shown in ***a***, highlighting individual cells (white arrows) in registered images.

770

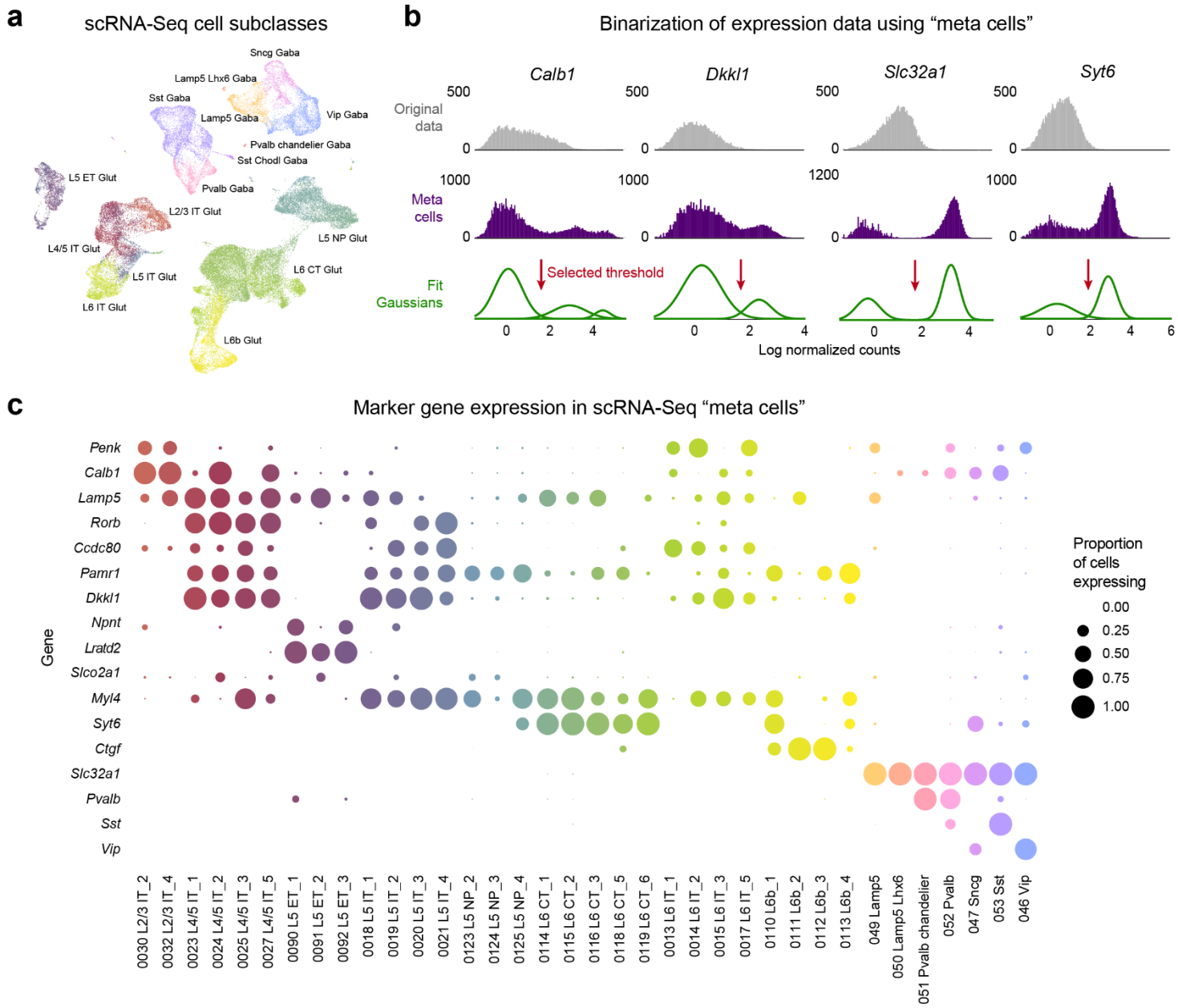

Extended Data Figure 4 – Binarization of scRNA-Seq marker gene expression data. (***a***) UMAP plot generated from ABC Atlas scRNA-Seq data, colored by cell subclass. (***b***) Example histograms for 4 marker genes showing original natural-log normalized counts distributions from ABC Atlas scRNA-Seq data (top, grey), log-norm counts distributions resulting from summing counts from 10 nearest-neighbor cells to create "meta cells" (middle, purple), and the gaussians fit to the meta cell distributions using gaussian mixture models (bottom, green). Gene expression binarization threshold is highlighted with a red arrow, indicating that cells with counts below or above the threshold were considered negative or positive for that gene, respectively. (***c***) Dot plot showing the proportion of excitatory cell supertypes and inhibitory cell subclasses expressing 17 marker genes. Only cell types found in ABC MERFISH data included. Dot size shows proportion of cells of each type expressing each gene.

771

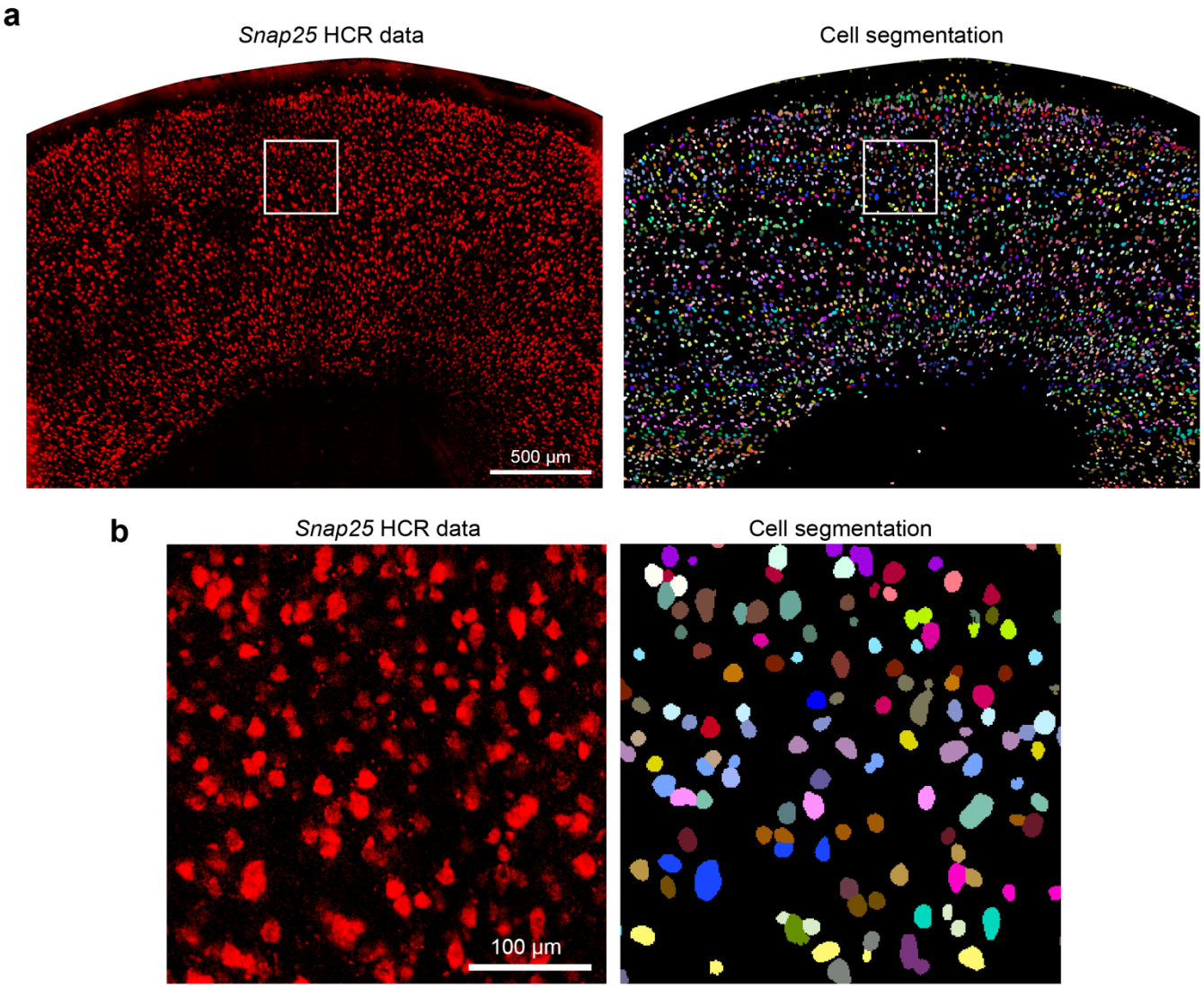

Extended Data Figure 5 – Cell segmentation using Snap25 signal and binary gene expression annotation across cell ROIs. (***a***) Confocal image of *Snap25* signal in a tissue section of dorsal cortex (left) alongside Cellpose3 segmentation of *Snap25* signal into individual cell ROIs (right). (***b***) Insets of images from ***a***. Cellpose3 allows segmentation of even densely labeled cells.

772

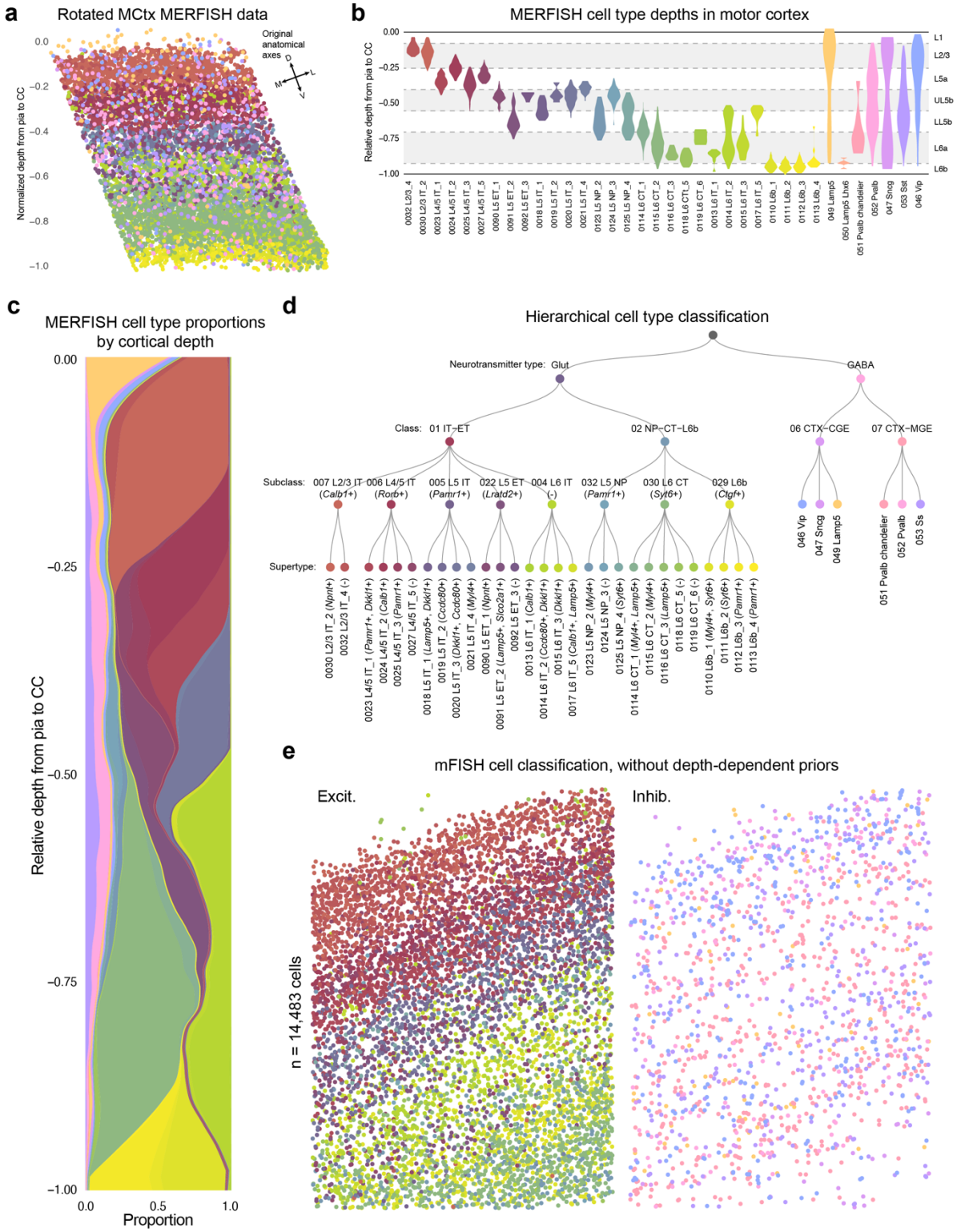

Extended Data Figure 6 – ABC MERFISH and scRNA-Seq data provide classification priors and test data. (***a***) Scatterplot showing arrangement of cells (dots) in ABC MERFISH data from the motor cortex, colored by cell type. Data have been rotated to provide a vertical axis to laminar arrangement of cell types. (***b***) Violin plots showing laminar arrangement of cells in ABC MERFISH data, grouped by excitatory supertypes and inhibitory subclasses used for classification of cells in our HCR mFISH data. Distributions show cells between the 1st and 99th percentiles of depth. (***c***) Relative cell type proportions across the full depth of motor cortex, determined from ABC MERFISH data, with a baseline probability of 0.2% applied to all cell types. At each depth, these proportions provided cell type prior probabilities for our Bayesian classifier. (***d***) Hierarchical tree of cell type classification derived from ABC transcriptomic data. Using our classifier, cells were classified along the hierarchy, first differentiating "neurotransmitter type", followed by "class", "subclass", and "supertype". Inhibitory cells were only classified down to the level of subclass. Excitatory supertypes are additionally annotated for marker genes that best distinguish them from their "sibling" cell types. (***e***) Scatterplots showing motor cortex cells (dots) imaged across 50 µm of z-depth in multi-round mFISH and classified into excitatory (left) or inhibitory (right) cell types based on gene expression patterns (n = 14,483 cells). Cell types were determined using a classifier that did not include depth-dependent cell type priors, in contrast to data shown in ***Fig. 3b***.

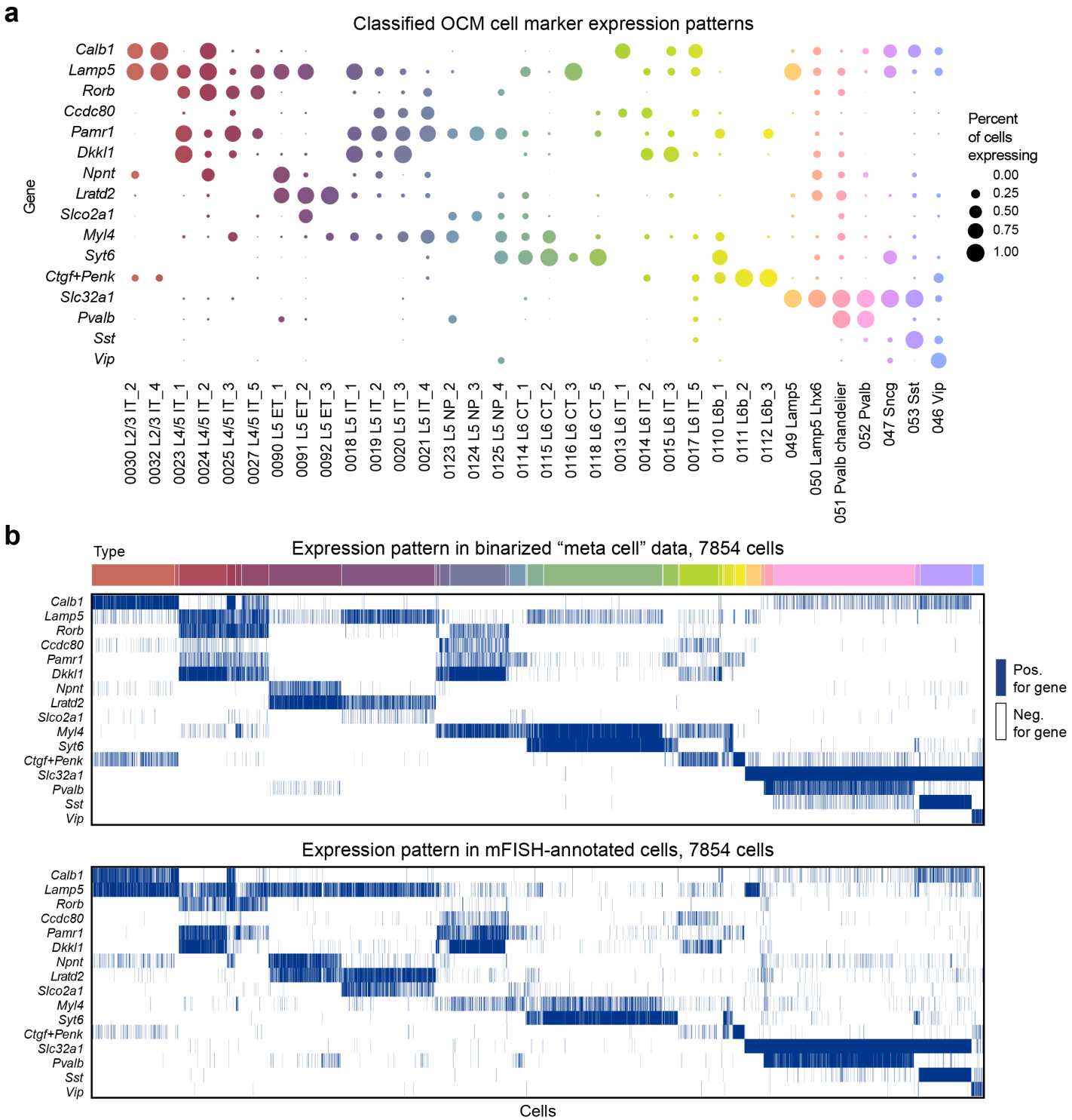

Extended Data Figure 7 – Gene expression patterns following classification of OCM-FISH data. (***a***) Dot plot shows marker gene expression patterns of our classified OCM-FISH cells. Dot size shows proportion of cells of each type expressing each gene. Only cell types with more than one cell are shown. (***b***) Heatmaps showing the binary expression pattern of marker genes across cells from scRNA-Seq "meta cells" (top) and from annotated OCM-FISH image data (bottom). Cells in the "meta cell" dataset were randomly selected to match the number of cells per type found in the OCM-FISH data (n = 7,854 cells). Blue indicates where cells were "positive" for a gene, with white indicating where cells were "negative" for a gene.

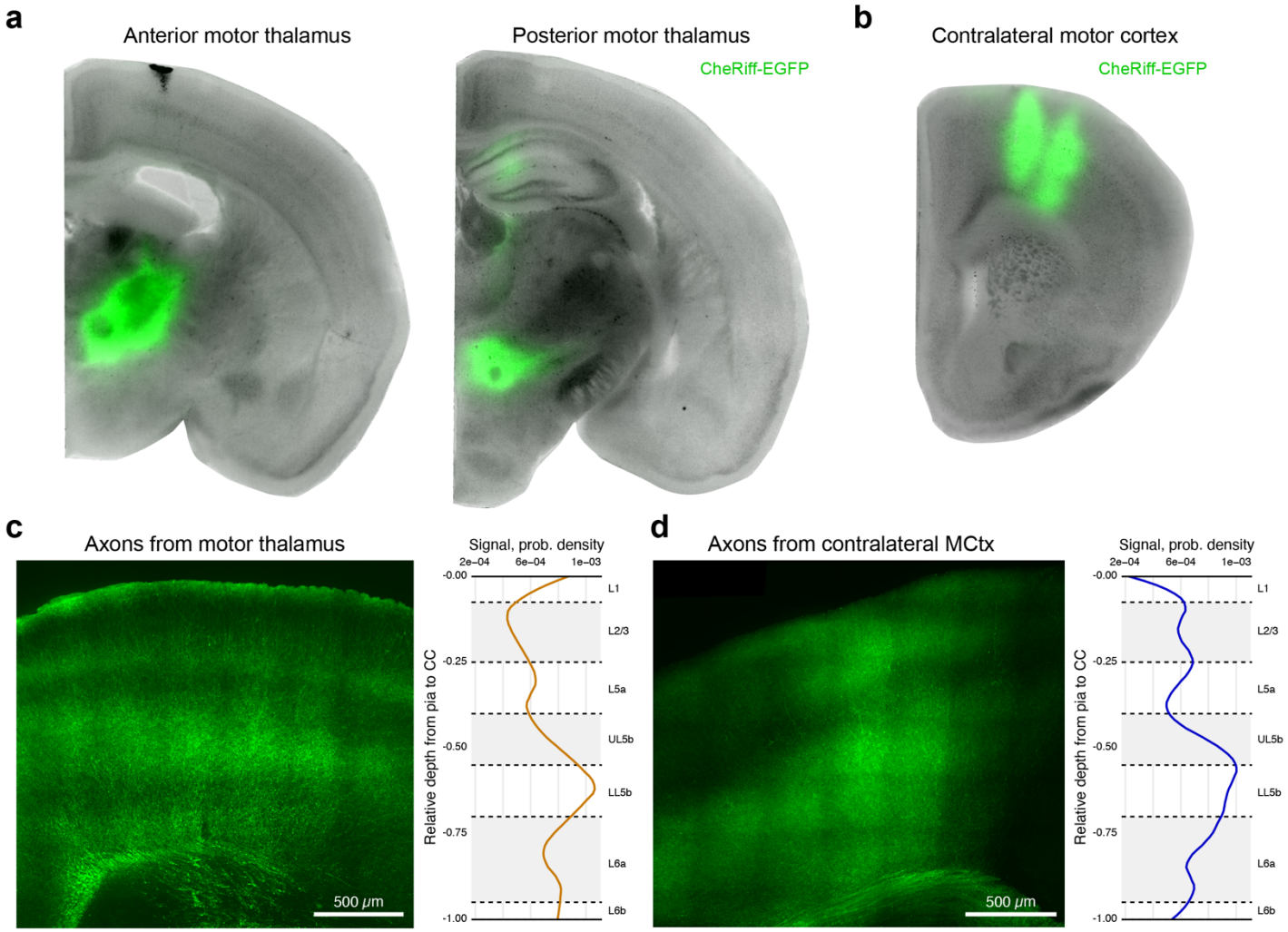

Extended Data Figure 8 – Injection site histology for AAV9-hSyn-CheRiff-EGFP delivery to MThal and contra motor cortex. (***a***) Representative images showing coronal hemisections with AAV9-hSyn-CheRiff-EGFP injections into anterior (left) and posterior (right) MThal. CheRiff-EGFP signal (green) is shown against tissue autofluorescence (grey). Nuclei showing expression include VAL and medial VM. (***b***) Representative image showing injections into two medial-lateral coordinates in contra motor cortex. Injections were additionally targeted to two cortical depths to achieve expression across cortical layers. (***c, d***) Representative image of CheRiff-EGFP-positive MThal axons (***c***) and contra motor cortex axons (***d***) in the ipsilateral motor cortex (left). EGFP signal density plots across cortical depths are shown on the right of each image.

775

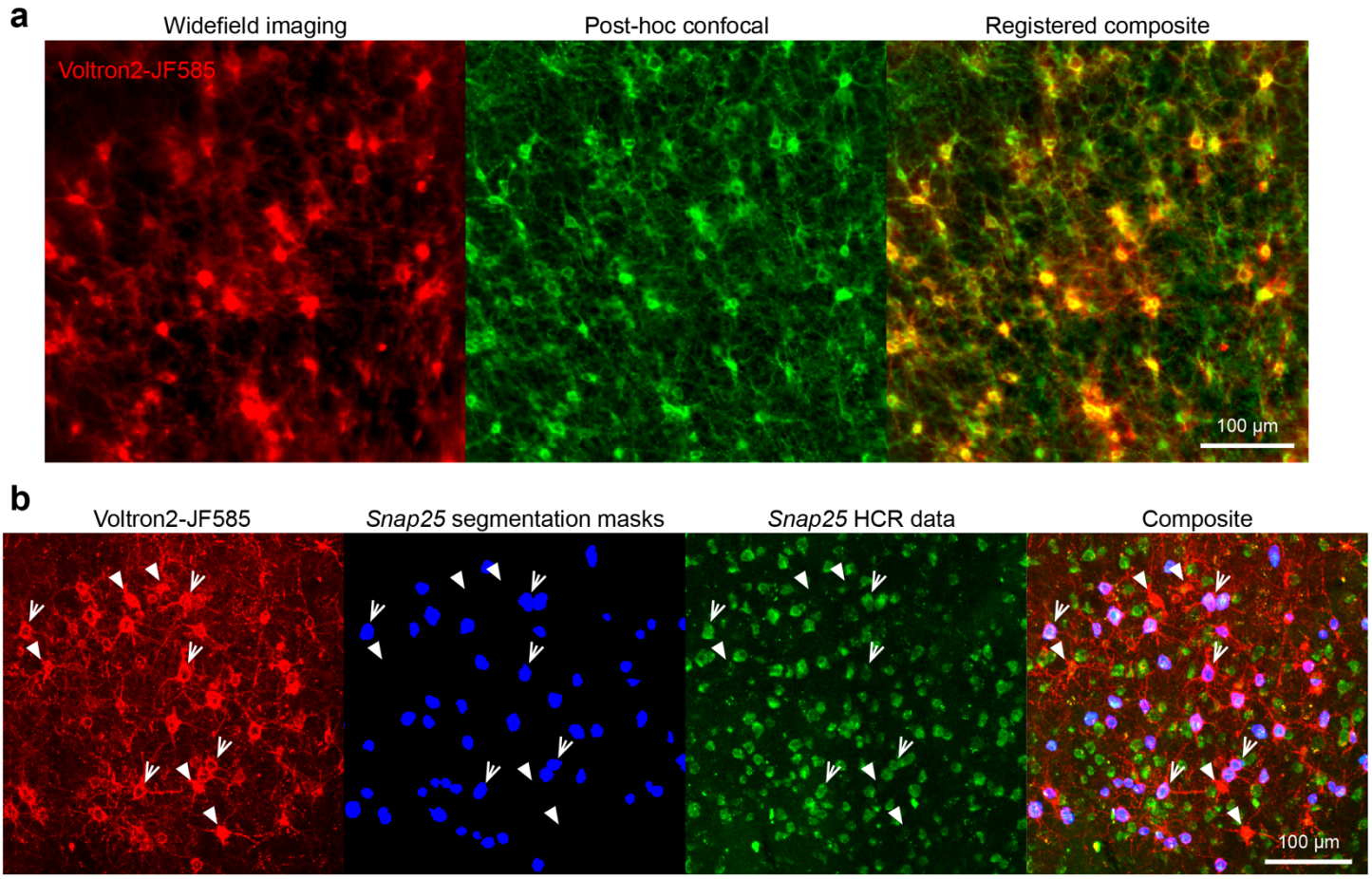

Extended Data Figure 9 – Segmentation and registration of Voltron2 image data in OCM-FISH. (***a***) Representative images showing widefield Voltron2-JF585 signal acquired during OCM (red), registered post-hoc Voltron2-JF585 confocal image used for mFISH histology (green), and image composite. (***b***) Image array showing a confocal histology image of Voltron2-expressing cells imaged in an OCM experiment (red), Snap25-based segmentation ROI masks annotated as Voltron2-positive (blue), Snap25 mFISH data used for cell segmentation (green), and composite image. Solid arrows highlight Voltron2-positive cells that did not show Snap25 signal and corresponding Snap25 segmentation masks, and dashed arrows show Voltron2-positive cells that had both.

776

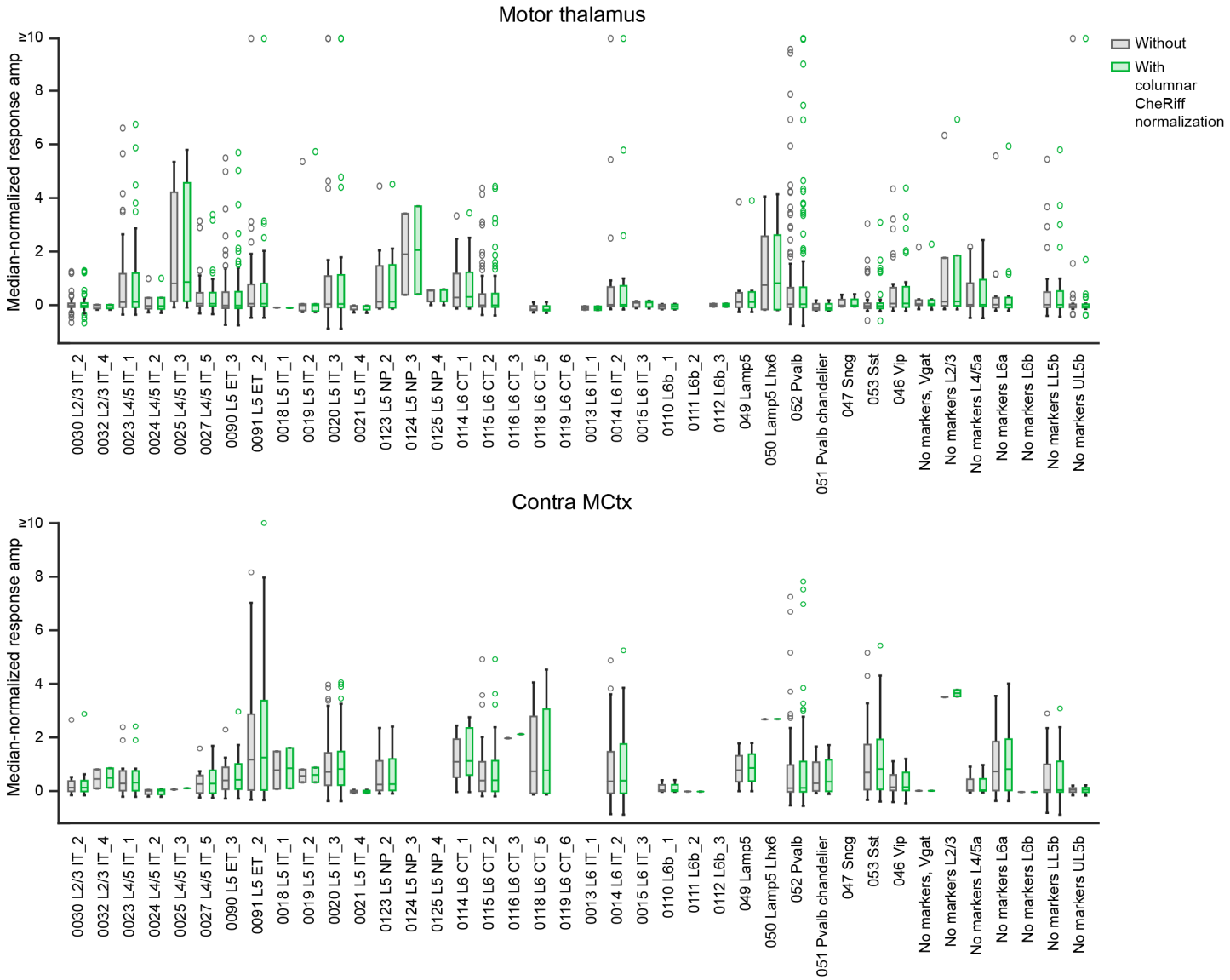

Extended Data Figure 10 – Normalized response amplitudes across cell types in OCM-FISH data. Box and whisker plots showing response amplitudes across cell types, normalized to just the median response amplitude in the same experimental slice (grey), or to both the median response amplitude and the relative CheRiff-EGFP signal found in the cell's cortical column (green). Data are shown for all MThal (top) and contra motor cortex (bottom) OCM-FISH experiments across cell types.

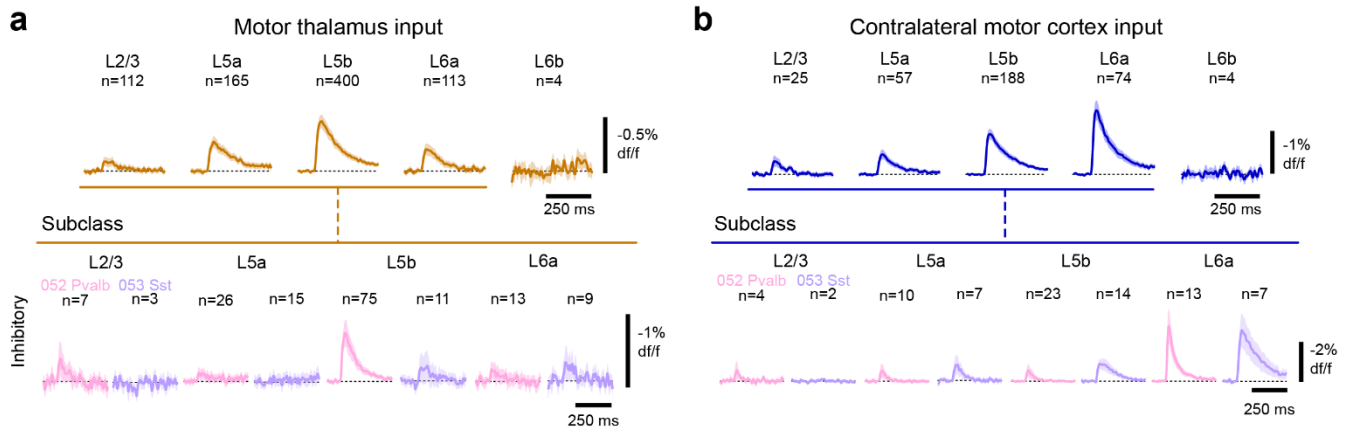

Extended Data Figure 11 – OCM-FISH data provide connectivity data for inhibitory cell types. (***a, b***) motor cortex PSPs resulting from activation of MThal inputs (***a***; orange) and contra motor cortex inputs (***b***; blue), grouped across all cell types by laminar depth (top), and across 052 Pvalb and 053 Sst inhibitory subclasses for cells found in L2/3-L6a (bottom). Line shows mean trace, shaded area shows SEM.

778